Direct Torque Control With Constant Switching Frequency for Three-to-Five Phase Direct Matrix Converter Fed Five-Phase Induction Motor Drive

Utkal Ranjan Muduli, *Member, IEEE*, Ranjan Kumar Behera, *Senior Member, IEEE*, Khalifa Al Hosani, *Senior Member, IEEE*, and Mohamed Shawky El Moursi, *Senior Member, IEEE*

***Abstract*—For heavy industrial drive applications, the direct matrix converter (DMC) solves the problems caused by the two-stage power conversion mechanism. Due to a lack of technological advancement, the control of multiphase drives operated by DMC is a significant cause of concern. This article thus presents a direct torque control (DTC) scheme based on space vector pulsewidth modulation (SVPWM) for a five-phase induction motor (FPIM) driven by a three-to-five (3×5) phase DMC. This proposed SVPWM-DTC employs the virtual vector (VV) concept to eliminate the effect of the xy component on 3×5 DMC output voltage space vectors. A novel approach is applied to analyze the effect of SVPWM-VV on the stator flux, torque, and speed of FPIM drive. Additionally, this SVPWM-VV regulates the input power factor of 3×5 DMC. The proposed work is simulated first and further validated by 3×5 DMC fed FPIM hardware prototype using field programmable gate array (FPGA)-based controller.**

***Index Terms*—Direct torque control (DTM), induction motor drives, matrix converter, power factor correction, space vector pulsewidth modulation (SVPWM).**

I. Introduction

IN MANUFACTURING industries, multiphase machine drive (MM) is gaining popularity due to its intrinsic fault-tolerant capability [1]. It is also suitable for application in the areas of electric vehicle (EV), electric aircraft, and marine drive applications in the high-power range [2]–[4]. Due to several advantages of the five-phase induction motor (FPIM) compared to other multiphase induction machines (IMs), it is considered in this article as a case study. As a result of intensive research on FPIM, it is currently available with some attractive features, such as reduced torque ripple, increased torque density, and lower power rating for each phase. A conventional two-stage power conversion process that involves a grid-side converter (GSC) and a load-side converter (LSC) is used to operate FPIM drives in heavy industries [4]. However, the direct matrix converter (DMC) fed FPIM drive is a single stage ac–ac power converter with significant advantages, such as controllable input power factor, sinusoidal input and output currents, bidirectional power flow, compact design [5].

A. Literature Review

To achieve high performance control, direct torque control (DTC), and field oriented control (FOC) have been investigated for the FPIM drive [6], [7]. Unlike FOC, DTC is superior for FPIM drive applications due to its better dynamic torque response, easy control algorithm, and insensitivity to variations in motor parameters [8], [9]. Two types of DTC structures, namely, look-up table (LUT)-based DTC and space vector pulsewidth modulation (SVPWM)-based DTC, are available in the literature. SVPWM-DTC shows better performance than LUT-DTC from the perspective of torque and flux ripple attenuation, as well as current harmonic mitigation [10], [11]. SVPWM-DTC has the characteristics of constant switching frequency, reduced torque ripple, reliable start-up, and improved low-speed operation [12]. Some DTC schemes intended for the DMC-fed three-phase induction motor (IM) or permanent magnet synchronous motor (PMSM) drive have been studied in various research papers [13]–[17]. Only a few publications are available for SVPWM-DTC operation for 3×3 phase DMC-fed IM and PMSM drives [16], [17]. However, their applicability to DMC-fed FPIM drives has not been investigated.

To represent the space vectors and the zero sequence component of a n-phase machine, $(n-1)/2$ space vector planes are required [4]. In FPIM, the fundamental components are represented in the $\alpha\beta$-plane and third harmonic components are represented in the xy-plane. Third harmonic components are undesirable in distributed stator wound FPIM, as they develop significant stator current distortions [18]. Therefore, to

Manuscript received November 13, 2021; revised March 4, 2022; accepted April 10, 2022. Date of publication April 14, 2022; date of current version May 23, 2022. This work was supported in part by the National Mission on Power Electronics Technology Project by the Ministry of Communications and Information Technology, Government of India, and by the Centre for Development of Advanced Computing, Thiruvananthapuram, India, under Grant NaMPET-Ph-III/SP26/NH-Exp-06/IITP, in part by Khalifa University, Abu Dhabi, UAE, under Grant KKJRC-2019-Trans2, and in part by the Advanced Technology Research Council ASPIRE Virtual Research Institute Program, Abu Dhabi, UAE, under Grant VRI20-07. Recommended for publication by Associate Editor M. Su. *(Corresponding author: Utkal Ranjan Muduli.)*

Utkal Ranjan Muduli, Khalifa Al Hosani, and Mohamed Shawky El Moursi are with the Advanced Power and Energy Center, Department of Electrical Engineering and Computer Science, Khalifa University, Abu Dhabi 127788, UAE (e-mail: utkal.muduli@ku.ac.ae; khalifa.halhosani@ku.ac.ae; mohamed.elmoursi@ku.ac.ae).

Ranjan Kumar Behera is with the Department of Electrical Engineering, Indian Institute of Technology Patna, Bihta, Bihar 801103, India (e-mail: rkb@iitp.ac.in).

Color versions of one or more figures in this article are available at https://doi.org/10.1109/TPEL.2022.3167477.

Digital Object Identifier 10.1109/TPEL.2022.3167477

neutralize the effects of the third harmonic components in FPIM, the resultant volt-second vector applied in a control interval must be zero in the xy-plane. In [18] and [19], the virtual vector (VV) technique has been applied to the FPIM drive to realize the resultant zero volt seconds. DTC approaches in [12] promise to significantly improve the performance of the FPIM drive fed by the voltage source inverter using a variety of VV combinations. There has been relatively little research done in the domain of multiphase systems powered by a DMC. Some recent research articles focus on the operation of an FPIM fed by a 3×5 phase DMC [20]–[22]. The control approaches are based on DTC [20], FOC [21], and model predictive control (MPC) [22]. The FOC approach in [21] exhibits a constant switching frequency operation of 3×5 DMC, while the DTC and MPC methods lead to a variable switching frequency operation of 3×5 DMC. As in the previous literature, it is well studied that FOC is much of the motor parameter dependent, leading to several uncertainties during motor operation. To eliminate such parameter variation, in this article a combined method is studied with the benefits of both DTC and SVPWM methods to obtain a desirable constant switching frequency of DMC with a reduced effect of parameter uncertainties. This article compares its performance with FOC-[21] to claim the benefits.

B. Motivation and Objectives

After carefully summarizing the existing solutions for DMC control, it can be concluded that the control problem of 3×5 DMC is still a fairly open topic and needs to be solved. The following facts support the proposed solution in this article.

1) The literatures are limited to GSC followed by the LSC-fed FPIM drive instead of the single-stage DMC converter. Furthermore, the SVPWM-DTC control available for 3×3 phase DMC cannot be extended to 3×5 phase DMC directly due to the presence of third-harmonic variables.
2) Different types of state space vectors, namely, null vectors, active vectors, and rotating vectors, are realizable in 3×5 DMC [5]. Although the rotating vectors generate no common mode voltage (CMV), the following problems are encountered, while using them for drive operation;
   a) as the direction of the rotating vectors is not fixed, the angle between adjoining vectors varies continuously, and hence the sector size between adjoining rotating vectors changes over time, and
   b) as the angular position of the rotating vector is rotating continuously at synchronous speed, the corresponding developed flux cannot be certainly evaluated.

Therefore, the output space voltage vectors (VV) need to be synthesized by employing either active vectors exclusively or sets of active and null vectors.

3) The active vectors are categorized into small, medium, and large vectors. Therefore, there is the possibility of several combinations of VV that can be implemented for the robust SVPWM-DTC based control approach of the 3×5 DMC fed FPIM drive.
4) Improper selection of VV may lead to performance degradation or even system damage; therefore, the impact of VV on the torque and flux performance of the particular FPIM must be investigated.
5) The power quality on the input side of the 3×5 DMC fed FPIM drive is the main issue in this investigation that needs to be mitigated by proper VV selection.

C. Contribution and article Organization

To address the drawbacks of existing approaches for controlling the 3×5 phase DMC-fed FPIM drive system, this article aims to design an SVPWM-DTC method consisting of a VV-based SVPWM strategy that possesses the following remarkable features.

1) An SVPWM scheme is developed using the large, medium, and null vectors. The concept of VV is incorporated into this SVPWM strategy to neutralize the effects of the voltage components in the xy plane.
2) The selected voltage VVs are used to maintain the constant switching frequency and provide maximum input voltage utilization to achieve the rated torque and a rated speed of the FPIM drive.
3) The theoretical analysis of the resultant voltage vector based on the proposed VV SVPWM is used to evaluate the performance of the drive flux and torque at a wide variety of speeds in the modulation range.
4) The inner loop of the DTC indirectly achieves better stator current performance in terms of ripple and %THD over a wide speed range.
5) The suggested SVPWM-DTC scheme exhibits the control action of the grid side current of 3×5 DMC in various power factor operations.
6) An experimental prototype is developed to validate the performance of the proposed SVPWM-DTC scheme in a wide range of speed operations.

To achieve these objectives, first, the dynamic modeling of 3×5 phase DMC with the proposed VV-SVPWM scheme is provided in $\alpha\beta$-stationary reference frame in Section II. After that, the maximum value of the modulation range and input power factor compensating angle are calculated. Then, in Section III, an SVPWM-DTC scheme is proposed based on the proposed VV-SVPWM strategy that is utilized to obtain the desired experimental performance in Section IV. Finally, Section V concludes article.

II. SVPWM Scheme for 3×5 DMC

The topology of a 3×5 phase DMC fed FPIM is depicted in Fig. 1, which has three input phases and five output phases. Each output phases of DMC are connected to all three input phases via a bidirectional IGBT switch. In such a way, 3×5 phase DMC require 15 bidirectional IGBT switches, where a total of 2^{15} permuted switching states are feasible using binary numbers {0,1}. The switching function $(S_{n_i n_o})$ is defined as "1" for the closed switch and "0" for the open switch. To achieve safe commutation, $S_{n_i n_o}$ is classified into a forward switching function $\left(S^{+}_{n_i n_o}\right)$ and backward switching function $\left(S^{-}_{n_i n_o}\right)$, as illustrated in Fig. 1. Here, the subscripts $n_i = \{a, b, c\}$ and $n_o = \{A, B, C, D, E\}$ denote the input phase and output phase,

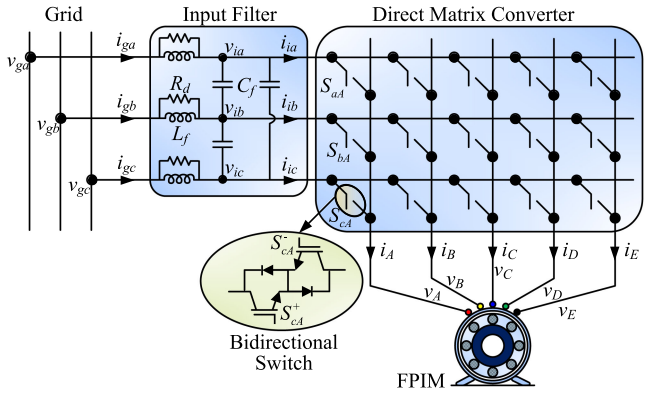

Fig. 1. 3×5 DMC fed FPIM topology using input *LC* filter.

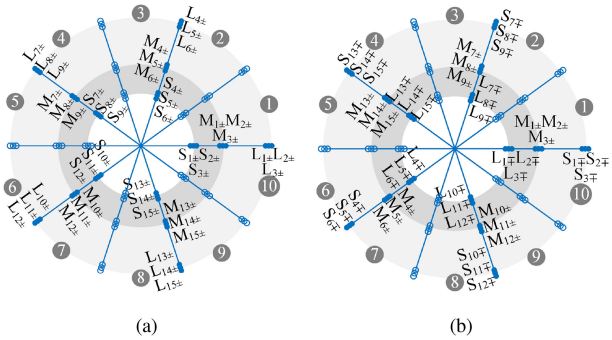

Fig. 2. Possible grouping of $\vec{v}_o^{\alpha\beta}$ vectors in (a) $\alpha\beta$ and (b) xy - plane.

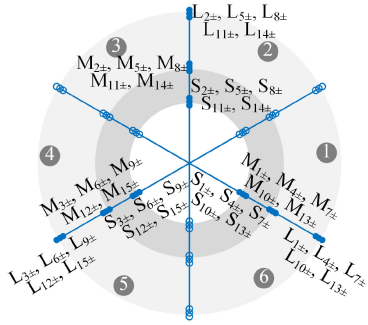

Fig. 3. Possible grouping of $\vec{i}_i^{\alpha\beta}$ vectors in $\alpha\beta$-plane.

respectively. The switching constraint for reliable operation of DMC is $S_{an_o} + S_{bn_o} + S_{cn_o} = 1$, which is to satisfy the following rules [5].

1) The input phase must not be short-circuited.
2) The output phase must not be open circuited for any switching instant.

Utilizing these constraints, a total 3^5 (243) potential switching combinations are possible. Symmetrical component theory, with its multiphase extension, leads to a 5-D representation of FPIM vector space with two mutually perpendicular 2-D subspaces ($\alpha\beta$ and xy-frame) and a zero subspace [23]. Generic variable X is utilized while transforming three-phase variables into two-phase stationary $\alpha\beta$-frame, as given in (1). Using the generic variable Y, it is convenient to transform the five-phase variables into two phase stationary $\alpha\beta$-frame and xy-frame for the theoretical analysis of FPIM, given in (2)

$$\begin{bmatrix} X^{\alpha\beta} \\ X^0 \end{bmatrix} = \frac{2}{3} \begin{bmatrix} \sum\limits_{m_i,n_i} a_i^{(m_i-1)} X_{n_i} \\ 0.5 \sum\limits_{n_i} X_{n_i} \end{bmatrix} \quad \begin{aligned} a_i &= e^{j2\pi/3} \\ m_i &\in \{1,2,3\} \\ n_i &\in \{a,b,c\} \end{aligned} \tag{1}$$

$$\begin{bmatrix} Y^{\alpha\beta} \\ Y^{xy} \\ Y^0 \end{bmatrix} = \frac{2}{5} \begin{bmatrix} \sum\limits_{m_o,n_o} a_o^{(m_o-1)} Y_{n_o} \\ \sum\limits_{m_o,n_o} a_o^{3(m_o-1)} Y_{n_o} \\ 0.5 \sum\limits_{n_o} Y_{n_o} \end{bmatrix}, \quad \begin{aligned} a_o &= e^{j2\pi/5} \\ m_o &\in \{1,2,3,4,5\} \\ n_o &\in \{A,B,C,D,E\} \end{aligned} \tag{2}$$

where m_i and m_o are considered as phase numbers.

A. Grouping of Vectors

All 243 switching combinations generate 243 current vectors in $\alpha\beta$-frame using (1) and 243 VV in both $\alpha\beta$ and xy-frame using (2). Out of which, 93 vectors (voltage or current) have variable magnitude and constant switching frequency in $\alpha\beta$-frame, whereas the other vectors cause variable magnitude, variable frequency, and dependency on the phase angle of the input voltage space vector. Thus, 93 VV in $\alpha\beta$ and xy-frames are useful for the proposed analysis, as shown in Fig. 2(a) and (b), respectively.

Similarly, the current vectors in $\alpha\beta$-frame are provided in Fig. 3. The useful vectors are subdivided into four groups as follows.

1) *Group I*: All output terminals are connected to the same input terminal of DMC. This group has three vectors that correspond to zero magnitude and are referred to as zero vectors.
2) *Group II*: Four of the output terminals are connected to the same input terminal of DMC. Total 30 vectors corresponding to this group have magnitude $0.47028 v_{il}$ and are called medium vectors. It means that the magnitude of output line voltage depends on 0.47028 ($= |M|$) times of the magnitude of the input line voltage ($v_{il} \in \{v_{ab}, v_{bc}, v_{ca}\}$).
3) *Group III*: Two adjacent output terminals are connected to the same input terminal of DMC. Total 30 vectors corresponding to this group have magnitude $0.76085 v_{il}$ and are called Large vectors. Here, the factor 0.76085 is represented as $|L|$.
4) *Group IV*: Two alternative output terminals are connected to the same input terminal of DMC. Total 30 vectors corresponding to this group have magnitude $0.29062 v_{il}$ and are called small vectors with factor $|S| = 0.29062$.

The large (L), medium (M), small (S), and zero (O) VV are represented in Table I with magnitude and phase angle of both output line voltage space vector $\left(\vec{v}_{ol}^{\alpha\beta}\right)$ and input current space vector $\left(\vec{i}_i^{\alpha\beta}\right)$. Now, $\vec{v}_{ol}^{\alpha\beta}$ can be obtained by

$$\vec{v}_{ol}^{\alpha\beta} = \frac{2}{5} \left[1 \; a_o \; a_o^2 \; a_o^3 \; a_o^4 \right] v_{ol} = \sqrt{2} v_o^* e^{j\left(\alpha_o^* + \frac{3\pi}{10}\right)} \tag{3}$$

TABLE I
USEFUL VOLTAGE VECTORS FOR 3×5 DMC ($|L| = 0.76085$, $|M| = 0.47028$, $|S| = 0.29062$)

Large Voltage Vectors						Medium Voltage Vectors						Small Voltage Vectors					
Switching States		$\vec{v}_{ol}^{\alpha\beta}$		$\vec{i}_i^{\alpha\beta}$		Switching States		$\vec{v}_{ol}^{\alpha\beta}$		$\vec{i}_i^{\alpha\beta}$		Switching States		$\vec{v}_{ol}^{\alpha\beta}$		$\vec{i}_i^{\alpha\beta}$	
State	ABCDE	$\frac{\lvert\vec{v}_{ol}^{\alpha\beta}\rvert}{\lvert L\rvert}$	α_o^*	$\frac{\sqrt{3}\lvert\vec{i}_i^{\alpha\beta}\rvert}{2\times1.618}$	β_i	State	ABCDE	$\frac{\lvert\vec{v}_{ol}^{\alpha\beta}\rvert}{\lvert M\rvert}$	α_o^*	$\frac{\sqrt{3}\lvert\vec{i}_i^{\alpha\beta}\rvert}{2}$	β_i	State	ABCDE	$\frac{\lvert\vec{v}_{ol}^{\alpha\beta}\rvert}{\lvert S\rvert}$	α_o^*	$\frac{\sqrt{3}\lvert\vec{i}_i^{\alpha\beta}\rvert}{2\times0.618}$	β_i
L_{1+}	aabba	v_{ab}	0	i_A	-$\pi/6$	M_{1+}	abbbb	v_{ab}	0	i_A	-$\pi/6$	S_{1+}	babba	v_{ab}	0	i_A	-$\pi/6$
L_{1-}	bbaab	v_{ab}	-π	i_A	$5\pi/6$	M_{1-}	baaaa	v_{ab}	-π	i_A	$5\pi/6$	S_{1-}	abaab	v_{ab}	-π	i_A	$5\pi/6$
L_{2+}	bbccb	v_{bc}	0	i_A	$\pi/2$	M_{2+}	bcccc	v_{bc}	0	i_A	$\pi/2$	S_{2+}	cbccb	v_{bc}	0	i_A	$\pi/2$
L_{2-}	ccbbc	v_{bc}	-π	i_A	-$\pi/2$	M_{2-}	cbbbb	v_{bc}	-π	i_A	-$\pi/2$	S_{2-}	bcbbc	v_{bc}	-π	i_A	-$\pi/2$
L_{3+}	ccaac	v_{ca}	0	i_A	-$5\pi/6$	M_{3+}	caaaa	v_{ca}	0	i_A	-$5\pi/6$	S_{3+}	acaac	v_{ca}	0	i_A	-$5\pi/6$
L_{3-}	aacca	v_{ca}	-π	i_A	$\pi/6$	M_{3-}	acccc	v_{ca}	-π	i_A	$\pi/6$	S_{3-}	cacca	v_{ca}	-π	i_A	$\pi/6$
L_{4+}	aaabb	v_{ab}	$2\pi/5$	i_B	-$\pi/6$	M_{4+}	babbb	v_{ab}	$2\pi/5$	i_B	-$\pi/6$	S_{4+}	ababb	v_{ab}	$2\pi/5$	i_B	-$\pi/6$
L_{4-}	bbbaa	v_{ab}	-$3\pi/5$	i_B	$5\pi/6$	M_{4-}	abaaa	v_{ab}	-$3\pi/5$	i_B	$5\pi/6$	S_{4-}	babaa	v_{ab}	-$3\pi/5$	i_B	$5\pi/6$
L_{5+}	bbbcc	v_{bc}	$2\pi/5$	i_B	$\pi/2$	M_{5+}	cbccc	v_{bc}	$2\pi/5$	i_B	$\pi/2$	S_{5+}	bcbcc	v_{bc}	$2\pi/5$	i_B	$\pi/2$
L_{5-}	cccbb	v_{bc}	-$3\pi/5$	i_B	-$\pi/2$	M_{5-}	bcbbb	v_{bc}	-$3\pi/5$	i_B	-$\pi/2$	S_{5-}	cbcbb	v_{bc}	-$3\pi/5$	i_B	-$\pi/2$
L_{6+}	cccaa	v_{ca}	$2\pi/5$	i_B	-$5\pi/6$	M_{6+}	acaaa	v_{ca}	$2\pi/5$	i_B	-$5\pi/6$	S_{6+}	cacaa	v_{ca}	$2\pi/5$	i_B	-$5\pi/6$
L_{6-}	aaacc	v_{ca}	-$3\pi/5$	i_B	$\pi/6$	M_{6-}	caccc	v_{ca}	-$3\pi/5$	i_B	$\pi/6$	S_{6-}	acacc	v_{ca}	-$3\pi/5$	i_B	$\pi/6$
L_{7+}	baaab	v_{ab}	$4\pi/5$	i_C	-$\pi/6$	M_{7+}	bbabb	v_{ab}	$4\pi/5$	i_C	-$\pi/6$	S_{7+}	babab	v_{ab}	$4\pi/5$	i_C	-$\pi/6$
L_{7-}	abbba	v_{ab}	-$\pi/5$	i_C	$5\pi/6$	M_{7-}	aabaa	v_{ab}	-$\pi/5$	i_C	$5\pi/6$	S_{7-}	ababa	v_{ab}	-$\pi/5$	i_C	$5\pi/6$
L_{8+}	cbbbc	v_{bc}	$4\pi/5$	i_C	$\pi/2$	M_{8+}	ccbcc	v_{bc}	$4\pi/5$	i_C	$\pi/2$	S_{8+}	cbcbc	v_{bc}	$4\pi/5$	i_C	$\pi/2$
L_{8-}	bcccb	v_{bc}	-$\pi/5$	i_C	-$\pi/2$	M_{8-}	bbcbb	v_{bc}	-$\pi/5$	i_C	-$\pi/2$	S_{8-}	bcbcb	v_{bc}	-$\pi/5$	i_C	-$\pi/2$
L_{9+}	accca	v_{ca}	$4\pi/5$	i_C	-$5\pi/6$	M_{9+}	aacaa	v_{ca}	$4\pi/5$	i_C	-$5\pi/6$	S_{9+}	acaca	v_{ca}	$4\pi/5$	i_C	-$5\pi/6$
L_{9-}	caaac	v_{ca}	-$\pi/5$	i_C	$\pi/6$	M_{9-}	ccacc	v_{ca}	-$\pi/5$	i_C	$\pi/6$	S_{9-}	cacac	v_{ca}	-$\pi/5$	i_C	$\pi/6$
L_{10+}	bbaaa	v_{ab}	-$4\pi/5$	i_D	-$\pi/6$	M_{10+}	bbbab	v_{ab}	-$4\pi/5$	i_D	-$\pi/6$	S_{10+}	bbaba	v_{ab}	-$4\pi/5$	i_D	-$\pi/6$
L_{10-}	aabbb	v_{ab}	$\pi/5$	i_D	$5\pi/6$	M_{10-}	aaaba	v_{ab}	$\pi/5$	i_D	$5\pi/6$	S_{10-}	aabab	v_{ab}	$\pi/5$	i_D	$5\pi/6$
L_{11+}	ccbbb	v_{bc}	-$4\pi/5$	i_D	$\pi/2$	M_{11+}	cccbc	v_{bc}	-$4\pi/5$	i_D	$\pi/2$	S_{11+}	ccbcb	v_{bc}	-$4\pi/5$	i_D	$\pi/2$
L_{11-}	bbccc	v_{bc}	$\pi/5$	i_D	-$\pi/2$	M_{11-}	bbbcb	v_{bc}	$\pi/5$	i_D	-$\pi/2$	S_{11-}	bbcbc	v_{bc}	$\pi/5$	i_D	-$\pi/2$
L_{12+}	aaccc	v_{ca}	-$4\pi/5$	i_D	-$5\pi/6$	M_{12+}	aaaca	v_{ca}	-$4\pi/5$	i_D	-$5\pi/6$	S_{12+}	aacac	v_{ca}	-$4\pi/5$	i_D	-$5\pi/6$
L_{12-}	ccaaa	v_{ca}	$\pi/5$	i_D	$\pi/6$	M_{12-}	cccac	v_{ca}	$\pi/5$	i_D	$\pi/6$	S_{12-}	ccaca	v_{ca}	$\pi/5$	i_D	$\pi/6$
L_{13+}	abbaa	v_{ab}	-$2\pi/5$	i_E	-$\pi/6$	M_{13+}	bbbba	v_{ab}	-$2\pi/5$	i_E	-$\pi/6$	S_{13+}	abbab	v_{ab}	-$2\pi/5$	i_E	-$\pi/6$
L_{13-}	baabb	v_{ab}	$3\pi/5$	i_E	$5\pi/6$	M_{13-}	aaaab	v_{ab}	$3\pi/5$	i_E	$5\pi/6$	S_{13-}	baaba	v_{ab}	$3\pi/5$	i_E	$5\pi/6$
L_{14+}	bccbb	v_{bc}	-$2\pi/5$	i_E	$\pi/2$	M_{14+}	ccccb	v_{bc}	-$2\pi/5$	i_E	$\pi/2$	S_{14+}	bcbcc	v_{bc}	-$2\pi/5$	i_E	$\pi/2$
L_{14-}	cbbcc	v_{bc}	$3\pi/5$	i_E	-$\pi/2$	M_{14-}	bbbbc	v_{bc}	$3\pi/5$	i_E	-$\pi/2$	S_{14-}	cbbcb	v_{bc}	$3\pi/5$	i_E	-$\pi/2$
L_{15+}	caacc	v_{ca}	-$2\pi/5$	i_E	-$5\pi/6$	M_{15+}	aaaac	v_{ca}	-$2\pi/5$	i_E	-$5\pi/6$	S_{15+}	caaca	v_{ca}	-$2\pi/5$	i_E	-$5\pi/6$
L_{15-}	accaa	v_{ca}	$3\pi/5$	i_E	$\pi/6$	M_{15-}	cccca	v_{ca}	$3\pi/5$	i_E	$\pi/6$	S_{15-}	accac	v_{ca}	$3\pi/5$	i_E	$\pi/6$
Zero Voltage Vectors																	
Oa	aaaaa	0	0	0	0	Ob	bbbbb	0	0	0	0	Oc	ccccc	0	0	0	0

where v_{ol} is the output line voltage of 3×5 phase DMC and can be represented as

$$v_{ol} = \begin{bmatrix} v_{AB} & v_{BC} & v_{CD} & v_{DE} & v_{EA} \end{bmatrix}^t = \sqrt{2} v_o^* \cos\left(\alpha_o^* + \frac{3\pi}{10} - \frac{2(m_o-1)\pi}{5}\right) \quad (4)$$

where v_o^* is the reference rms output line voltage, $\alpha_o^* (= \omega_o^* t + \varphi_v^*)$ is the reference displacement angle of the output voltage; ω_o^* is the reference output angular frequency; and φ_v^* is the reference phase angle of the output phase voltage. Each of the output line voltages are constructed from the output pole voltages (v_{pn_o}) or output phase voltages (v_{n_o}). The output phase voltage of DMC can be expressed as the difference of the pole voltage and the common mode voltage (v_{cm}) appeared at the output terminal, i.e., $v_{n_o} = v_{pn_o} - v_{cm}$. The common mode voltage and the output pole voltage can be represented as

$$v_{cm} = \frac{1}{5}\sum_{n_o} v_{pn_o} \quad \text{and} \quad v_{pn_o} = \sum_{n_i} S_{n_i n_o} v_{gn_i} \quad (5)$$

where v_{gn_i} is considered as the input phase voltage with instantaneous value of $\sqrt{\frac{2}{3}} V_i \cos\left(\alpha_i - \frac{2(m_i-1)\pi}{3}\right)$ and the switching function $S_{n_i n_o}$ is defined earlier in this section. $\alpha_i (= \omega_i t + \varphi_v)$ and V_i are the phase and rms value of the input line voltage, respectively. ω_i and φ_v are the input angular frequency and displacement angle of the input voltage, respectively. The input phase voltage space vector $\left(\vec{v}_i^{\alpha\beta}\right)$ and the output phase voltage space vector $\left(\vec{v}_o^{\alpha\beta}\right)$ can be obtained using (1) and (2) and are shown in Fig. 4(a) and (b), respectively. For further analysis of the modulation scheme, the representation of input current space

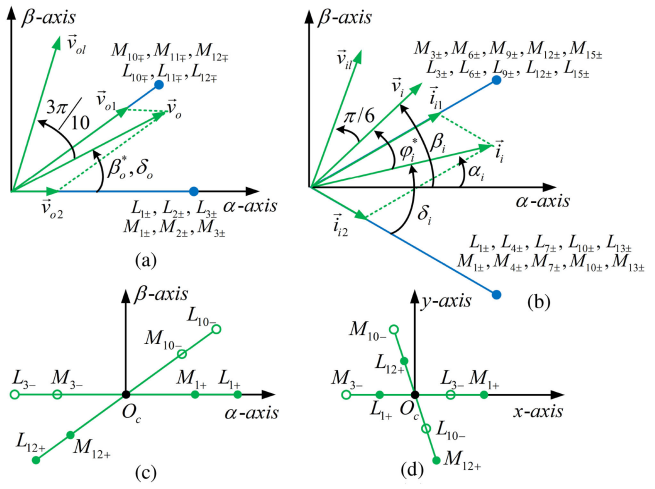

Fig. 4. Representation of (a) $v_o^{\alpha\beta}$ (b) $i_i^{\alpha\beta}$; proposed vectors for sector-1 in (c) $\alpha\beta$-plane and (d) xy-plane.

TABLE II
DWELL TIMES FOR THE PROPOSED SVPWM SCHEME

$d_{1L}=\frac{5}{3}\,\lvert L\rvert\,\zeta_i m_a \sin\delta_v \sin\left(\frac{\pi}{3}-\delta_i\right)$	$d_{1M}=\frac{5}{3}\,\lvert M\rvert\,\zeta_i m_a \sin\delta_v \sin\left(\frac{\pi}{3}-\delta_i\right)$
$d_{2L}=\frac{5}{3}\,\lvert L\rvert\,\zeta_i m_a \sin\delta_v \sin\delta_i$	$d_{2M}=\frac{5}{3}\,\lvert M\rvert\,\zeta_i m_a \sin\delta_v \sin\delta_i$
$d_{3L}=\frac{5}{3}\,\lvert L\rvert\,\zeta_i m_a \sin\left(\frac{\pi}{5}-\delta_v\right) \sin\left(\frac{\pi}{3}-\delta_i\right)$	$d_{3M}=\frac{5}{3}\,\lvert M\rvert\,\zeta_i m_a \sin\left(\frac{\pi}{5}-\delta_v\right) \sin\left(\frac{\pi}{3}-\delta_i\right)$
$d_{4L}=\frac{5}{3}\,\lvert L\rvert\,\zeta_i m_a \sin\left(\frac{\pi}{5}-\delta_v\right) \sin\delta_i$	$d_{4M}=\frac{5}{3}\,\lvert M\rvert\,\zeta_i m_a \sin\left(\frac{\pi}{5}-\delta_v\right) \sin\delta_i$
$d_0=1-(d_{1L}+d_{2L}+d_{3L}+d_{4L}+d_{1M}+d_{2M}+d_{3M}+d_{4M})$	

vector $\left(\vec{i}_i^{\alpha\beta}\right)$ is necessary, which can be obtained as

$$\vec{i}_i^{\alpha\beta}=\frac{2}{3}\sum_{m_i,n_i} a_i^{(m_i-1)} i_{in_i}=\sqrt{2}I_i e^{j\beta_i} \tag{6}$$

where i_{in_i} represents input phase current of DMC with instantaneous value $i_{in_i}=\sqrt{2}I_i\cos\left(\beta_i-\frac{2k\pi}{3}\right)$. The phase β_i $(=\omega_i t+\varphi_i^*)$ has the reference current displacement angle of φ_i^*. I_i represents the rms value of the input current of the DMC. Instead of directly measuring i_{in_i}, it can be obtained from the output phase current (i_{n_o}) of DMC and the switching function as

$$i_{in_i}=\sum_{n_o} S_{n_i n_o} i_{n_o}. \tag{7}$$

The five-phase output current of 3×5 phase DMC fed FPIM and its space vector in $\alpha-\beta$ reference frame are given by

$$\vec{i}_o^{\alpha\beta}=\frac{2}{3}\left[\,1\;a_o\;a_o^2\;a_o^3\;a_o^4\,\right] i_{n_o}=\sqrt{2}I_o e^{j\beta_o} \tag{8}$$

where $i_{n_o}=\sqrt{2}I_o\cos\left(\beta_o-\frac{2k\pi}{5}\right)$ is the instantaneous output phase current; β_o $(=\omega_o^* t+\varphi_i)$, φ_i, and I_o represent the phase, displacement angle, and rms value of the output current, respectively.

The VV for the SVPWM scheme need to be arranged in a sequence such that the average volt-second of the complete sequence in a switching time instant T_{sw} is zero. It nullifies the effect of xy-component of output voltage $(\vec{v}_o^{xy})$ and current $\left(\vec{i}_o^{xy}\right)$ on the various performances of the connected load. Such VV concept is analyzed for SVPWM scheme in this section, which is referred further as SVPWM-VV. The SVPWM-VV utilizes the original voltage vector and its dwell times to determine the resultant voltage space vector. Dwell time for each voltage vector of 3×5 DMC can be computed as Table II to regulate the input power factor and minimize the %THD of output current. $\{d_{1L},\, d_{2L},\, d_{3L},\, \text{and}\;\, d_{4L}\}$ represent dwell times correspond to the large VV and the dwell times $\{d_{1M},\, d_{2M},\, d_{3M},\, \text{and}\;\, d_{4M}\}$ are assigned for medium VV. Here, $m_a(=v_o^*/V_i)$ is the modulation index and the variable $\zeta_i=(\cos\varphi_g)^{-1}$ depend on the input power factor; $\varphi_g=\varphi_v-\varphi_i^*$ is the input power factor angle. $0\le\delta_v\le\pi/5$ and $0\le\delta_i\le\pi/3$ represent the dwell angle of $\vec{v}_o^{\alpha\beta}$ and $\vec{i}_i^{\alpha\beta}$, and represented in Fig. 4(a) and (b), respectively.

B. Formation of SVPWM-VVs

1) VVs in $\alpha\beta$-Frame: The output voltage space vector $\left(\vec{v}_o^{\alpha\beta}\right)$ constitutes ten sectors with $\pi^c/5$ per sector, as shown in Fig. 2(a). Similarly, Fig. 3 shows six input current sectors of $\vec{i}_i^{\alpha\beta}$ with $\pi^c/3$ per sector. Let $k_v\in\{1,2,\ldots,10\}$ and $k_i\in\{1,2,\ldots,6\}$ be the variables representing sectors of $\vec{v}_o^{\alpha\beta}$ and $\vec{i}_i^{\alpha\beta}$, respectively. Utilizing k_v and k_i, totally 60 different VV combinations are possible. If k_v+k_i is an odd number, then the dwell time sequence of $d_{1M}-d_{3L}-d_{1L}-d_{3M}-d_{4M}-d_{2L}-d_{4L}-d_{2M}-d_0$ is utilized; otherwise, sequence $d_{3M}-d_{1L}-d_{3L}-d_{1M}-d_{2M}-d_{4L}-d_{2L}-d_{4M}-d_0$ is being useful.

TABLE III
LUT FOR SVPWM SCHEME FOR 3×5 DMC

Sector of $\vec{v}_{ol}^{\alpha\beta}$	Sector of $\vec{i}_{il}^{\alpha\beta}$		
	1 or 4	2 or 5	3 or 6
1 or 6	$M_{1\pm}$, $L_{10\pm}$, $L_{1\pm}$ $M_{10\pm}$, $M_{12\pm}$, $L_{3\pm}$ $L_{12\pm}$, $M_{3\pm}$, O_c	$M_{12\pm}$, $L_{3\pm}$, $L_{12\pm}$ $M_{3\pm}$, $M_{2\pm}$, $L_{11\pm}$ $L_{2\pm}$, $M_{11\pm}$, O_b	$M_{2\pm}$, $L_{11\pm}$, $L_{2\pm}$ $M_{11\pm}$, $M_{10\pm}$, $L_{1\pm}$ $L_{10\pm}$, $M_{1\pm}$, O_a
2 or 7	$M_{4\pm}$, $L_{10\pm}$, $L_{4\pm}$ $M_{10\pm}$, $M_{12\pm}$, $L_{6\pm}$ $L_{12\pm}$, $M_{6\pm}$, O_c	$M_{12\pm}$, $L_{6\pm}$, $L_{12\pm}$ $M_{6\pm}$, $M_{5\pm}$, $L_{11\pm}$ $L_{5\pm}$, $M_{11\pm}$, O_b	$M_{5\pm}$, $L_{11\pm}$, $L_{5\pm}$ $M_{11\pm}$, $M_{10\pm}$, $L_{4\pm}$ $L_{10\pm}$, $M_{4\pm}$, O_a
3 or 8	$M_{4\pm}$, $L_{13\pm}$, $L_{4\pm}$ $M_{13\pm}$, $M_{15\pm}$, $L_{6\pm}$ $L_{15\pm}$, $M_{6\pm}$, O_c	$M_{15\pm}$, $L_{6\pm}$, $L_{15\pm}$ $M_{6\pm}$, $M_{5\pm}$, $L_{14\pm}$ $L_{5\pm}$, $M_{14\pm}$, O_b	$M_{5\pm}$, $L_{14\pm}$, $L_{5\pm}$ $M_{14\pm}$, $M_{13\pm}$, $L_{4\pm}$ $L_{13\pm}$, $M_{4\pm}$, O_a
4 or 9	$M_{7\pm}$, $L_{13\pm}$, $L_{7\pm}$ $M_{13\pm}$, $M_{15\pm}$, $L_{9\pm}$ $L_{15\pm}$, $M_{9\pm}$, O_c	$M_{15\pm}$, $L_{9\pm}$, $L_{15\pm}$ $M_{9\pm}$, $M_{8\pm}$, $L_{14\pm}$ $L_{8\pm}$, $M_{14\pm}$, O_b	$M_{8\pm}$, $L_{14\pm}$, $L_{8\pm}$ $M_{14\pm}$, $M_{13\pm}$, $L_{7\pm}$ $L_{13\pm}$, $M_{7\pm}$, O_a
5 or 10	$M_{7\pm}$, $L_{1\pm}$, $L_{7\pm}$ $M_{1\pm}$, $M_{3\pm}$, $L_{9\pm}$ $L_{3\pm}$, $M_{9\pm}$, O_c	$M_{3\pm}$, $L_{9\pm}$, $L_{3\pm}$ $M_{9\pm}$, $M_{8\pm}$, $L_{2\pm}$ $L_{8\pm}$, $M_{2\pm}$, O_b	$M_{8\pm}$, $L_{2\pm}$, $L_{8\pm}$ $M_{2\pm}$, $M_{1\pm}$, $L_{7\pm}$ $L_{1\pm}$, $M_{7\pm}$, O_a

The sequence of these VVs with large and medium VV can be obtained from Table III. Assume that both $\vec{v}_o^{\alpha\beta}$ and $\vec{i}_i^{\alpha\beta}$ are in sector-1 (i.e., $k_v=1$ and $k_i=1$), as shown in Fig. 4(a) and (b). As per Fig. 4(a), $\vec{v}_o^{\alpha\beta}$ can be computed using the components $\vec{v}_{o1}^{\alpha\beta}$ and $\vec{v}_{o2}^{\alpha\beta}$. Similarly, $\vec{i}_i^{\alpha\beta}$ can be constructed from vector addition of $\vec{i}_{i1}^{\alpha\beta}$ and $\vec{i}_{i2}^{\alpha\beta}$, as shown in Fig. 4(b). $\{V_{L1\pm}, V_{M1\pm}\}$, $\{V_{L3\pm}, V_{M3\pm}\}$, $\{V_{L10\mp}, V_{M10\mp}\}$, and $\{V_{L12\mp}, V_{M12\mp}\}$ are the common VV that are being used to synthesize $\vec{v}_o^{\alpha\beta}$ and $\vec{i}_i^{\alpha\beta}$. As per the output current and input voltage direction during $k_v=1$ and $k_i=1$ and also to maintain a constant switching frequency with a minimum number of switching transitions, $\{V_{M1+}, V_{L10-}, V_{L1+}, V_{M10-}, V_{M12+}, V_{L3-}, V_{L12+}, V_{M3-}, V_{Oc}\}$ is considered useful in $\alpha\beta$-plane, as shown in Fig. 4(c). These vectors can be illustrated as Fig. 4(d) in xy-plane. As $k_v+k_i=2$ (i.e., even number), the dwell time sequence $d_{3M}-d_{1L}-d_{3L}-d_{1M}-d_{2M}-d_{4L}-d_{2L}-d_{4M}-d_0$ is chosen. This output voltage synthesization during $k_v=1$ and $k_i=1$ can be illustrated in Fig. 5. Here, T_{sw} (i.e., $1/f_{sw}$) is the switching period of the complete sequence with the carrier switching frequency f_{sw}. An optional state O_a can be inserted in between the above sequence to control the v_{cm} of the 3×5 DMC phase voltage, which is not detailed here. The VV $V_{M1+}, V_{L10-}, V_{L1+}, V_{M10-}$ are utilized for formation of $\vec{v}_{o1}^{\alpha\beta}$, whereas VV V_{M12+}, V_{L3-}, V_{L12+}, and V_{M3-} are forming $\vec{v}_{o2}^{\alpha\beta}$, as of (9) and (10), respectively

$$\begin{aligned}\vec{v}_{o1}^{\alpha\beta}&=d_{1L}V_{L10-}^{\alpha\beta}+d_{1M}V_{M10-}^{\alpha\beta}+d_{2M}V_{M12+}^{\alpha\beta}+d_{2L}V_{L12+}^{\alpha\beta}\\&=d_{1L}\left(\lvert L\rvert\, v_{ab}e^{j\pi/5}\right)+d_{1M}\left(\lvert M\rvert\, v_{ab}e^{j\pi/5}\right)\\&\quad+d_{2M}\left(\lvert M\rvert\, v_{ca}e^{-j4\pi/5}\right)+d_{2L}\left(\lvert L\rvert\, v_{ca}e^{-j4\pi/5}\right)\end{aligned} \tag{9}$$

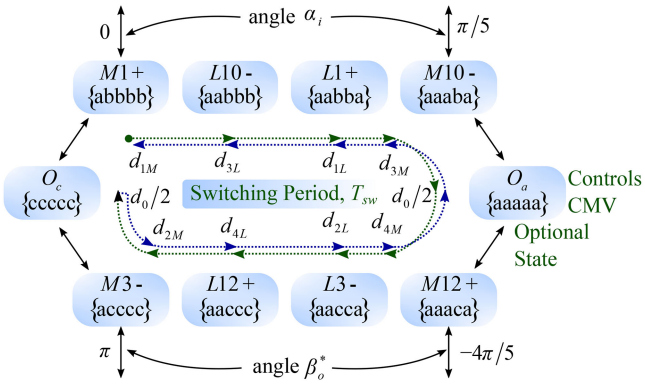

Fig. 5. DMC output voltage synthesization diagram at $k_v = 1$ & $k_i = 1$.

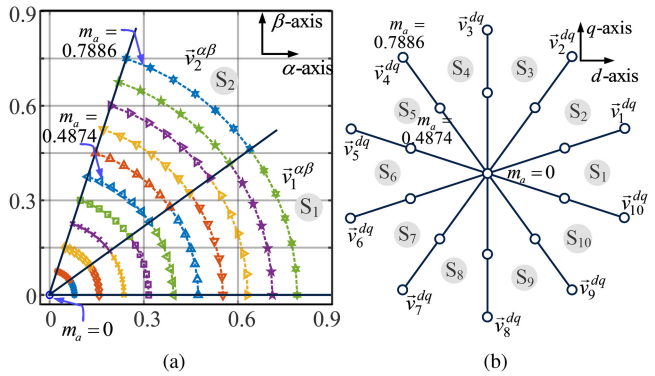

Fig. 6. Possible VV representation in (a) $\alpha\beta$-frame and (b) dq-frame.

$$= \left[\begin{pmatrix} |L|\, d_{1L} \\ +|M|\, d_{1M} \end{pmatrix} v_{ab} - \begin{pmatrix} |M|\, d_{2M} \\ +|L|\, d_{2L} \end{pmatrix} v_{ca} \right] e^{j\pi/5}$$

$$\vec{v}_{o2}^{\alpha\beta} = d_{3M} V_{M1+}^{\alpha\beta} + d_{3L} V_{L1+}^{\alpha\beta} + d_{4L} V_{L3-}^{\alpha\beta} + d_{4M} V_{M3-}^{\alpha\beta}$$
$$= d_{3M} \left(|M|\, v_{ab} e^{j0} \right) + d_{3L} \left(|L|\, v_{ab} e^{j0} \right)$$
$$+ d_{4L} \left(|L|\, v_{ca} e^{-j\pi} \right) + d_{4M} \left(|M|\, v_{ca} e^{-j\pi} \right)$$
$$= \left[\begin{pmatrix} |M|\, d_{3M} \\ +|L|\, d_{3L} \end{pmatrix} v_{ab} - \begin{pmatrix} |L|\, d_{4L} \\ +|M|\, d_{4M} \end{pmatrix} v_{ca} \right] e^{j0}. \quad (10)$$

By utilizing the defined values of the input line voltages v_{ab} $\left(= \sqrt{2} V_i \cos(\alpha_i + \frac{\pi}{6})\right)$ and v_{ca} $\left(= \sqrt{2} V_i \cos(\alpha_i - \frac{\pi}{2})\right)$, voltage vector components $\vec{v}_{o1}^{\alpha\beta}$ and $\vec{v}_{o2}^{\alpha\beta}$ can be calculated. From Fig. 4(a), the resultant voltage virtual vector $\vec{v}_1^{\alpha\beta}$ ($\vec{v}_o^{\alpha\beta}$ in sector-1) can be mentioned as

$$\vec{v}_1^{\alpha\beta} = \vec{v}_{o1}^{\alpha\beta} + \vec{v}_{o2}^{\alpha\beta} = m_a V_i e^{j(\delta_v + \pi/10)}. \quad (11)$$

It can be seen from (11) that the output voltage VV is independent of the input phase angle (φ_g) at the switching time instant T_{sw}. Hence, the motor torque and flux variation will not be affected by the variation of φ_g. It is only dependent on the input line voltage magnitude, i.e., V_i. Again, with the proposed SVPWM dwell time, the virtual vector corresponding to xy-plane is nullified as (14). Hence, the xy-components of the stator flux harmonics do not affect the overall performance of the load

$$\vec{v}_{o1}^{xy} = d_{1L} V_{L10-}^{xy} + d_{1M} V_{M10-}^{xy} + d_{2M} V_{M12+}^{xy} + d_{2L} V_{L12+}^{xy} \quad (12)$$

$$\vec{v}_{o2}^{xy} = d_{3M} V_{M1+}^{xy} + d_{3L} V_{L1+}^{xy} + d_{4L} V_{L3-}^{xy} + d_{4M} V_{M3-}^{xy} \quad (13)$$

$$\vec{v}_1^{xy} = \vec{v}_{01}^{xy} + \vec{v}_{02}^{xy} = 0. \quad (14)$$

In Fig. 6(a), VV $\vec{v}_1^{\alpha\beta}$ is represented for $0 \le m_a \le 0.7886$ and $0 \le \delta_v \le \pi/5$ in sector-1 of $\vec{v}_o^{\alpha\beta}$. By using a similar analysis as of (11), the magnitude and angle of $(k_v)^{th}$ VV for SVPWM scheme can be computed in $\alpha\beta$-frame as

$$\vec{v}_{k_v}^{\alpha\beta} = m_a V_i e^{j(\delta_v + k_v \pi/10)} \quad n \in \{1, 2 \ldots 10\}. \quad (15)$$

Only 10 VVs can be possible for all 60 combinations of sector positions. The redundancy of VVs position occurs as VVs phase and/or angle does not depend on φ_g.

2) VVs in dq-Frame: Through angular transformation, $v_{k_v}^{\alpha\beta}$ can be converted to VVs ($v_{k_v}^{dq}$) in a synchronously rotating dq-frame by

$$\vec{v}_{k_v}^{dq} = \vec{v}_{k_v}^{\alpha\beta} e^{-j\delta_v} = m_a V_i e^{jk_v\pi/10}, \quad n \in \{1, 2 \ldots 10\}. \quad (16)$$

Again, it can be seen from (16) that $\vec{v}_{k_v}^{dq}$ $(= v_{k_v}^{d} + j v_{k_v}^{q})$ is independent of δ_v and varies only due to m_a. It is positioned at $+k_v\pi/10$ in an anticlockwise manner and shown in Fig. 6(b).

C. Computation of Maximum Values of m_a and φ_g

The SVPWM scheme only can be validated while maintaining d_0 to positive value, i.e., $d_0 \ge 0$. Now, the feasible solution for the modulation index (m_a) can be obtained as

$$m_a \le \frac{\cos\varphi_g}{\frac{4}{3}\sin\left(\frac{2\pi}{5}\right)\cos\left(\frac{\pi}{10} - \delta_v\right)\cos\left(\frac{\pi}{6} - \delta_i\right)}. \quad (17)$$

The maximum value of m_a can be achieved as (18) by using trigonometric inequalities, i.e., $\cos(\frac{\pi}{10} - \delta_v)\cos(\frac{\pi}{6} - \delta_i) \to 1$ for $\delta_v = \frac{\pi}{10}$ and $\delta_i = \frac{\pi}{6}$

$$m_a \le \frac{\cos\varphi_g}{\frac{4}{3}\sin\left(\frac{2\pi}{5}\right)}. \quad (18)$$

The modulation index varies in the interval of $m_a \in (0, 0.7886]$, where $m_a = 0.7886$ is obtained corresponding to the unity power factor operation of the grid current with $\varphi_g \approx 0$. As observed from (18), each m_a corresponds to a maximum compensation of φ_g. However, the proposed SVPWM scheme is only feasible if $\vec{v}_i$ leads $\vec{i}_i$ to one sector, i.e., $\varphi_g \le \pi/3$. The maximum value of φ_g ($\varphi_{g,\max}$) can be obtained as

$$\varphi_{g,\max} = \begin{cases} \cos^{-1}\left(\frac{4m_a}{3}\sin\left(\frac{2\pi}{5}\right)\right), & 0.3943 < m_a \le 0.7886 \\ \frac{\pi}{3}, & 0 < m_a \le 0.3943. \end{cases} \quad (19)$$

The relation between $\varphi_{g,\max}$ and m_a can be graphically represented in Fig. 7. This graph depicts the accessibility of the output voltage vector at different load demand.

D. Commutation of 3×5 DMC Switches

Power converter modulation schemes have a direct impact on commutation losses, and the proposed SVPWM scheme assures a minimum switching count for each vector transition.

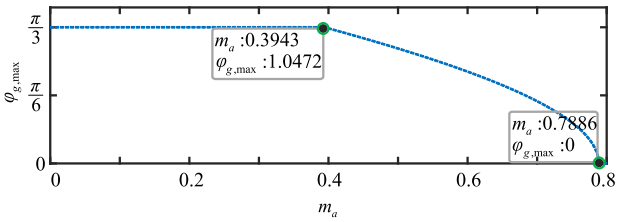

Fig. 7. Relationship curve for m_a and $\varphi_{g,\max}$.

The commutation losses can be reduced further by selecting an appropriate VV sequence in a sector. The product of differential voltage level (Δv_{gn_i}) and the current i_{n_o} through each bidirectional IGBT switch approximately settles the effective power losses in a certain commutation. Each DMC transition must always involve two switches with the same output phase: one to turn OFF and the other to turn ON. Because real-world commutations cannot be instantaneous, unique bidirectional switches with two distinct gates for each current direction are required to avoid shorting the voltage sources or opening the current source (see Fig. 1). In any instance, the voltage or current sign must be known in order to select the appropriate switching sequence. In the traditional four-step commutation method with voltage-controlled and current-controlled techniques, proper sign detection is an issue, while Δv_{gn_i} and i_{n_o} are near to zero [24]. Hence, the proposed algorithm is utilized with either voltage or current commutation in each step to prevent critical transitions, which entails switching with Δv_{gn_i} or i_{n_o} below the set threshold values. For safe commutation, the threshold values of Δv_{gn_i} and i_{n_o} are kept as 15 V and 0.5 A, respectively. The time interval between each consecutive step is set at $T_d = 1.5\,\mu s$. This value is determined by the power semiconductor devices' turn-ON/OFF characteristics. To assess the efficacy of this technique, a safety ratio corresponding to Δv_{gn_i} divided by the threshold voltage needs to obtain if the commutation is voltage regulated, or i_{n_o} divided by the threshold current if it is current controlled. As a result, this ratio determines the safety margin of each commutation, with anything greater than one, indicating that the commutation is safe. Because there is no current freewheeling channel in DMC, dependable current commutation between bidirectional switches is difficult to build. The current flowing through the switches must be actively managed, and numerous commutation strategies have been described for good functioning [25]. The gate pulse waveform during voltage commutation with either $v_{ga} > v_{gb}$ or $v_{ga} < v_{gb}$ are indicated in Fig. 8(a) and (b), respectively. Fig. 8(c) and (d) depict the gate pulse waveforms generated by FPGA-based implementation in the case of positive and negative output phase-A current i_A, respectively, during the current commutation.

III. Proposed Control Methodology

An SVPWM-DTC scheme for 3×5 DMC fed FPIM is proposed in this section. The proposed scheme utilizes the resultant SVPWM VV for the analysis of stator flux and torque variation along with the maintenance of the input power factor, i.e., zero phase angle difference between the grid voltage and

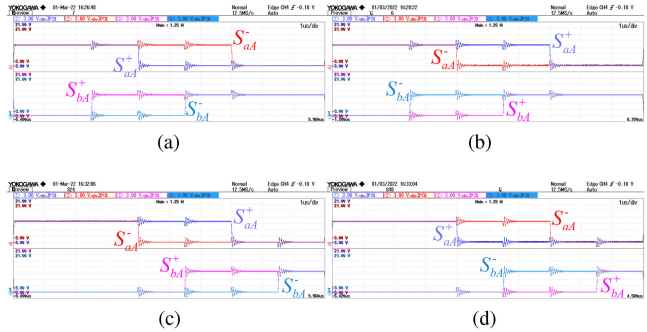

Fig. 8. Gate pulse $\left\{S^+_{aA}, S^-_{aA}, S^+_{bA}, S^-_{bA}\right\}$ waveforms generated by FPGA-based implementation considering both voltage and current commutations. (a) Voltage commutation, $v_{ga} > v_{gb}$. (b) Voltage commutation, $v_{ga} < v_{gb}$. (c) Current commutation, $i_A > 0$. (d) Current commutation, $i_A < 0$.

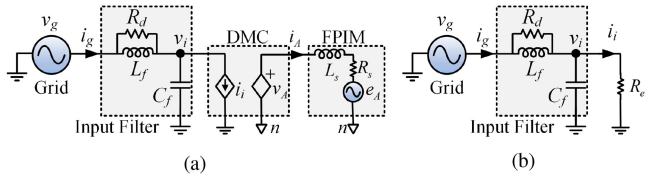

Fig. 9. (a) Equivalent diagram of DMC fed FPIM for input phase-a and output phase-A. (b) Simplified model of input side of DMC for filter design.

point-of-common-coupling (PCC) current. The conventional FPIM drive in [18] utilizes the DTC scheme, which cancels the torque production due to the components of stator flux and stator current in xy-plane. However, this scheme cannot be directly implemented for 3×5 DMC fed FPIM drive to achieve in-phase grid voltage and current simultaneously. Hence, a detailed study of phase compensation is presented in this section along with the effect of VVs on %change in flux, %change in torque, and speed variation.

A. Input Power Factor Compensation

The design and analysis of the input filter parameters are important aspects for the input power factor compensation of the DMC. Fig. 9 shows the modeling of the DMC with the input LC-filter. DMC can be modelled as R_e, which is the ratio of the magnitude of fundamental input voltage (V_i) and input current (I_i) of the DMC [26]. R_d is the resistance of the damping resistor. L_f and C_f denote the inductance and capacitance of the LC-filter, respectively. Utilizing the model in Fig. 9(b), the transfer function $G(s)$ ($=i_i(s)/v_g(s)$) can be obtained as

$$G(s) = \frac{1}{R_e} \frac{\frac{\omega_0}{Q_c} s + \omega_0^2}{s^2 + \frac{\omega_0}{Q_e} s + \omega_0^2} \tag{20}$$

where $Q_c \left(= \frac{1}{R_d}\sqrt{\frac{L_f}{C_f}}\right)$ and $Q_e \left(= \frac{R_d R_e}{R_d + R_e}\sqrt{\frac{C_f}{L_f}}\right)$ are the quality factors of the LC-filter; $\omega_0 \left(= \frac{1}{\sqrt{L_f C_f}}\right)$ is the resonant angular frequency of the LC-filter. The filter parameters and its characteristics affect the input power factor angle (φ_g) of the

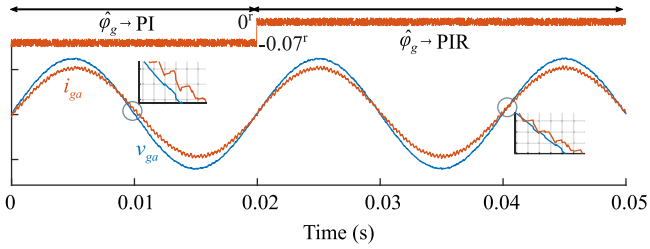

Fig. 10. Performance of estimated $\hat{\varphi}_g$ with PI and PIR.

DMC. The estimation of φ_g ($\hat{\varphi}_g$) can be written as [26]

$$\hat{\varphi}_g = \tan^{-1}\left[\omega_g C_f R_e\right] + \tan^{-1}\left[\frac{\omega_g L_f}{R_d}\right] - \tan^{-1}\left[\frac{\omega_g L_f}{1-\omega_g^2 L_f C_f}\frac{(R_d+R_e)}{R_d R_e}\right]. \quad (21)$$

It can be seen from (21) that $\hat{\varphi}_g$ depends on the various parameters of the input filter. Hence, the parameter variation may affect the accurate estimation of $\hat{\varphi}_g$. To overcome the issue due to parameter variation, a simplified approach with proportional-integral (PI)-based controller can be implemented to estimate $\hat{\varphi}_g$[27]. The PI compensation controller can be denoted as (22) by utilizing the error variable $\Delta\varphi_g(=\sin(\varphi_g^*)-\sin(\varphi_g))$

$$\hat{\varphi}_g = \left|\left(k_p + \frac{k_i}{s}\right)\Delta\varphi_g\right|_{-\varphi_{g,\max}}^{\varphi_{g,\max}} \quad (22)$$

where k_p and k_i are proportional and integral constants of PI controller, respectively. The use of PI controller can achieve a desirable steady-state value of $\hat{\varphi}_g$. It has the inability to track the phase angle with higher accuracy, as the transfer function $G(s)$ is a second-order system. To nullify the effects due to second-order system on the tracking of $\hat{\varphi}_g$, a resonant term is added to the existing PI controller in (22). The resonant frequency (ω_r) of the resonant controller is set to twice the grid frequency, i.e., $\omega_r = 2\omega_g$, without affecting the high-frequency stability of the DMC. To avoid the instability due to the grid frequency variation and discretization errors, a damping term needs to be added to the traditional resonant controller. The resultant proportional-integral-resonant (PIR) controller for the input power factor compensation can be written as

$$\hat{\varphi}_g = \left|\left(k_p + \frac{k_i}{s} + k_r\frac{k_d\frac{\omega_r}{Q_d}s}{s^2 + k_d\frac{\omega_r}{Q_d}s + \omega_r^2}\right)\Delta\varphi_g\right|_{-\varphi_{g,\max}}^{\varphi_{g,\max}} \quad (23)$$

where k_r and k_d are the resonant controller gain and damped gain. Q_d is the quality factor of the damped term of the resonant controller. Approximately 0.07^c phase error can be observed with PI-based regulator, while PIR compensation technique give desired phase detection with minimal steady-state error. The respective performance with both PI and PIR compensation techniques can be visualized from Fig. 10. Now, the final estimation of ζ_i can be obtained using $\hat{\varphi}_g$, i.e., $\zeta_i = (\cos\hat{\varphi}_g)^{-1}$.

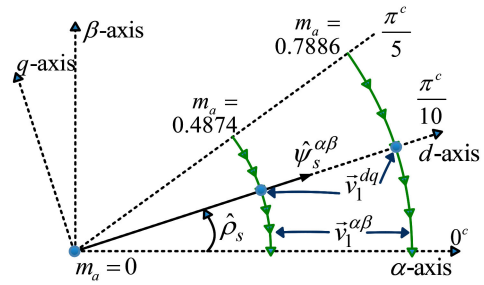

Fig. 11. Representation of $\hat{\psi}^s_{\alpha\beta}$ in $\alpha\beta$-frame and dq-frame.

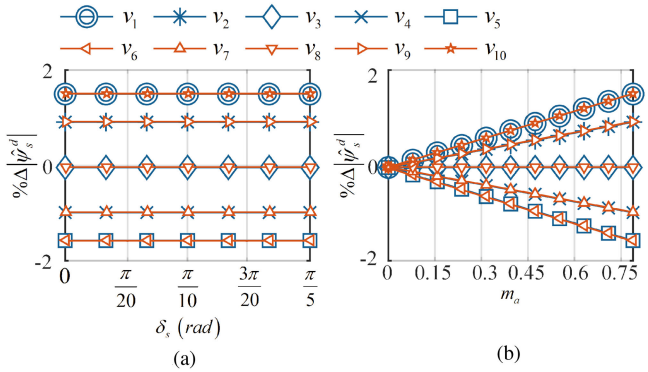

Fig. 12. Impacts of VVs on (a) $\%\,\Delta|\hat{\psi}^s_{\alpha\beta}|$ for $-\pi/10 \le \delta_o \le \pi/10$ at $m_a = 0.7886$ (b) $\%\,\Delta|\hat{\psi}^s_{\alpha\beta}|$ for $0 \le m_a \le 0.7886$ at $\delta_o = \pi/10$ rad in dq-frame.

B. Effect of SVPWM-VV on FPIM Performance

For analyzing the effect of SVPWM VV on FPIM performance, all five-phase quantities are initially transformed to $\alpha\beta$-frame by considering $Y \in \{v,\, i,\, \psi\}$ in (2). Afterward, $Y_o^{\alpha\beta}$ is converted to Y_o^{dq} in synchronously rotating dq-frame by using

$$\vec{Y}_o^{dq} = Y_o^d + jY_o^q = \vec{Y}_o^{\alpha\beta}e^{-j\theta_o}. \quad (24)$$

The estimated stator flux in $\alpha\beta$-frame can be mentioned as $\hat{\psi}_s^{\alpha\beta} = \hat{\psi}_s^{\alpha} + j\hat{\psi}_s^{\beta} = |\hat{\psi}_s^{\alpha\beta}|e^{j\hat{\rho}_s}$, where $|\hat{\psi}_s^{\alpha\beta}|$ and $\hat{\rho}_s$ denote the magnitude and phase angle of $\hat{\psi}_s^{\alpha\beta}$. The effect of SVPWM VV on stator flux $\left(\hat{\psi}_s^{dq} = \hat{\psi}_s^d + j\hat{\psi}_s^d\right)$ in dq-frame can be analyzed by considering sector-1 of $\hat{\rho}_s$, as shown in Fig. 11. For simplification, $\hat{\psi}_s^q$ is considered as null and $\hat{\psi}_s^d$ is fully contributed to development of $\hat{\psi}_s^{dq}$. Now, the change in $\hat{\psi}_s^d$ $\left(\Delta\hat{\psi}_s^d\right)$ over a switching period T_{sw} can be derived as

$$\Delta\hat{\psi}_s^d = T_{dtc}\left(v_{k_v}^d - R_s i_o^d\right) \quad (25)$$

where $v_{k_v}^d$ and i_o^d are the d-axis $(k_v)^{th}$-sector SVPWM VV and deviation in stator current $\left(\hat{i}_o^{dq} = i_o^d + ji_o^d\right)$, respectively. R_s denotes the dc resistance of the stator. Now, the $\%\,\Delta\hat{\psi}_s^d$ attains constant magnitude in the interval $0 \le \rho_s \le \pi/5$ for a specific m_a, as shown in Fig. 12(a). As $v_{k_v}^d$ directly depends on m_a, $\%\,\Delta\hat{\psi}_s^d$ magnitude proportionately increases for the interval $0 \le m_a \le 0.7886$ that can be investigated from Fig. 12(b). Furthermore, the electromagnetic torque $\left(\hat{T}_e\right)$ can be expressed

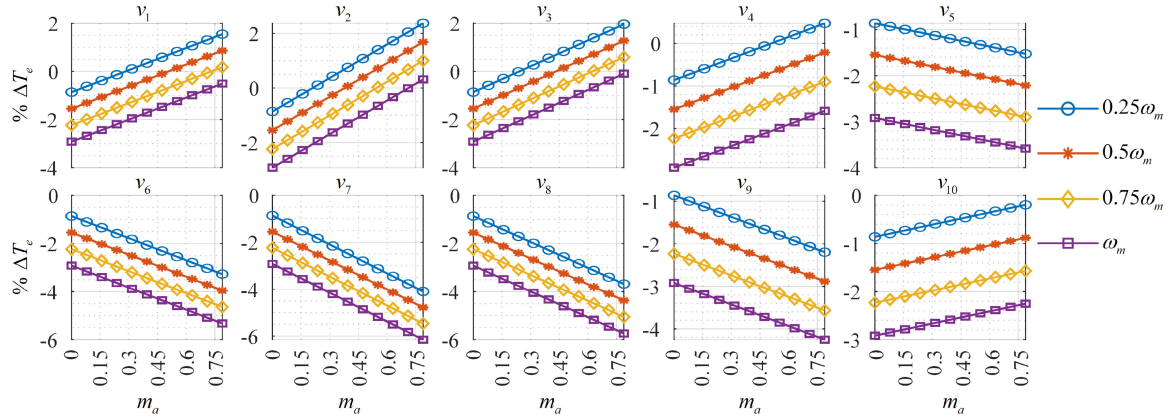

Fig. 13. Impact VVs on $\%\,\Delta T_e$ for $0 \leq m_a \leq 0.7886$ at $\delta_o = \pi/10$ rad.

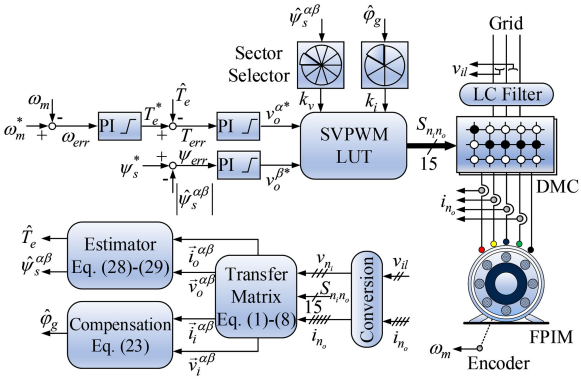

Fig. 14. SVPWM-DTC operation of FPTL-VSI fed FPIM drive.

as (26) in dq-frame by considering $\hat{\psi}_q^s = 0$

$$\hat{T}_e = k_t\left(\hat{\psi}_s^d i_o^q - \hat{\psi}_s^q i_o^d\right) = k_t \hat{\psi}_s^d i_o^q \tag{26}$$

where k_t $(= (5/2)(P/2))$ and P denote the torque constant and number of poles of FPIM. A small perturbation in $\hat{\psi}_s^d$ and i_o^q deviate $\hat{T}_e$. The deviation in $\hat{T}_e$ $\left(\Delta\hat{T}_e\right)$ can be obtained as (27) by utilizing the change in i_o^q, i.e., $\Delta i_o^q = T_{sw}(v_{k_v}^q - R_s i_o^q - \omega_r \hat{\psi}_s^d)/2\sigma L_s$

$$\Delta\hat{T}_e = k\psi_n \Delta i_o^q + \frac{T_e}{\psi_n}\Delta\hat{\psi}_s^d \tag{27}$$

where ψ_n, L_s, L_r, and L_m represent the nominal flux, stator leakage inductance, rotor leakage inductance, and magnetizing inductance of FPIM, respectively. σ $(= 1 - L_m^2/L_s L_r)$ denotes the magnetizing coefficient of FPIM. ω_r $(= (P/2)\omega_m)$ and ω_m are the electrical rotor speed and actual motor speed in r/min, respectively. It is revealed from (27) that $\Delta\hat{T}_e$ is indirectly affected by the modulation index (m_a) of the SVPWM-VVs and speed (ω_m) of the motor. For the interval of $0 \leq m_a \leq 0.7886$, the impact of SVPWM-VVs on $\%\Delta\hat{T}_e$ is examined from Fig. 13. Offline analysis is performed for 25%, 50%, 75%, and 100% of rated ω_m (i.e., $\omega_n = 2\pi f_n$, f_n is the nominal frequency of FPIM), while maintaining the load torque (T_L) to the rated value (T_n), i.e., $100\%T_n$. For instance, VV $\hat{v}_2^{dq}$ has positive $\%\,\Delta T_e$ for 100% ω_n at $m_a = 0.7254$, while the flux angle $\hat{\rho}_s$ is at $\pi/10$. Hence, the proposed controller selects $\hat{v}_2^{dq}$ for the production of motor torque in sector-2. From the similar analysis, it can be seen that $\hat{v}_1^{dq} \ldots \hat{v}_4^{dq}$ are suitable for low speed operation of 25% ω_n, as these VVs have positive $\%\,\Delta\hat{T}_e$. However, $\hat{v}_2^{dq}$ is the most preferable at 25% ω_n as the desired speed can be achievable at lower m_a of 0.1734. With the selection of $\hat{v}_2^{dq}$ in sector-2, $100\% - 125\%$ of ω_n can be achievable in a linear modulation range of $0.7254 \leq m_a \leq 0.7886$. The torque performance severely impacts for $0 < m_a < 0.1734$, i.e., during the low speed region of less than 25% ω_n. It is possible to conclude that a wide range of speed can be achieved across the linear modulation range.

C. Proposed SVPWM-DTC

For high-performance and reliable FPIM drive operation, DTC technique is commonly advantageous in terms of complexity and parameter sensitivity [18]. Less computational complexity, lower parameter sensitivity, minimal switching losses, and constant switching frequency operation are among the benefits of SVPWM-DTC scheme. Fig. 14 depicts the generalized structure of the proposed SVPWM-DTC operated 3×5 DMC fed FPIM drive. The steps to achieve the required performance with the proposed controller are summarized as follows.

Step 1: Measure v_{in_i}, i_{n_o}, and ω_m by using three voltage sensors, five current sensors, and one speed encoder.

Step 2: Take the feedback of the internally generated switching pulse $S_{n_i n_o}$ with unit delay and generate v_{n_o}, i_{in_i} as per (5) and (7).

Step 3: Convert v_{in_i}, i_{in_i} i_{n_o}, and v_{n_o} to $v_i^{\alpha\beta}$, $i_i^{\alpha\beta}$, $v_o^{\alpha\beta}$, and $i_o^{\alpha\beta}$, respectively, by using $\alpha\beta$-transformation relations (1) and (2).

Step 4: Estimate the stator flux $\left(\hat{\psi}_{\alpha\beta}^s\right)$ as (28) and electromagnetic torque $\left(\hat{T}_e\right)$ as

$$\hat{\psi}_s^{\alpha\beta} = \int_0^t \left(\vec{v}_o^{\alpha\beta} - R_s \vec{i}_o^{\alpha\beta}\right) dt \tag{28}$$

$$\hat{T}_e = k\left|\hat{\psi}_s^{\alpha\beta}\right|\left|\vec{i}_o^{\alpha\beta}\right|\sin(\rho_s - \beta_o). \tag{29}$$

Step 5: Calculate the torque reference (T_e^*) by utilizing a PI controller, which is being used to track ω_m with the reference speed ω_m^*. k_p^ω, and k_i^ω are the proportional and integral constants of the speed controller.

Step 6: Obtain the stator flux reference (ψ_s^*) from ω_m. ψ_s^* maintains to ψ_n for below the rated ω_m and varies inversely with ω_m for above the rated ω_m.

Step 7: Compare the estimated value of $\hat{T}_e$ $\left(|\hat{\psi}^s_{\alpha\beta}|\right)$ with T_e^* (ψ_s^*) to produce torque error T_{err} (flux error, ψ_{err}), respectively.

Step 8: Utilize two separate PI regulators to track T_{err} and ψ_{err}, which further produces v_o^{q*} and v_o^{d*}, respectively. k_p^d and k_i^d (k_p^q and k_i^q) are the proportional and integral constants of the d-axis (q-axis) current controller.

Step 9: Convert the reference voltage space vector $\left(\vec{v}_o^{dq*} = v_o^{d*} + jv_o^{q*}\right)$ to $\vec{v}_o^{\alpha\beta*}$ as (30) by utilizing estimated stator flux angle $\hat{\rho}_s$

$$\vec{v}_o^{\alpha\beta*} = \left|\vec{v}_o^{\alpha\beta*}\right| e^{j\delta_v} = \vec{v}_o^{dq*} e^{j\hat{\rho}_s}. \tag{30}$$

Step 10: Calculate $\hat{\varphi}_g$ as per (23) for input power compensation. Furthermore, utilize $\hat{\varphi}_g$, the effective angle of $\vec{v}_o^{\alpha\beta*}$ (i.e., δ_v) and δ_i for the computation of the dwell time of the proposed SVPWM as per Table II.

Step 11: Compute the sector (k_v and k_i) by utilizing δ_v and δ_i to select the appropriate VV from Table III.

Step 12: Generate switching states $S_{n_i n_o}$ $(n_i \in \{a, b, c\}, n_o \in \{A, B, C, D, E\})$ in accordance with Table I to guarantee the constant switching frequency operation.

The selection of the error amplifier gains is determined in relation to the actual motor parameters for providing better sensitivity. Specified delay has been introduced in each interpreted block in Fig. 14 to achieve real-time performance.

IV. Results and Discussions

A. Experimental Prototype Description

The theoretical analysis of the proposed SVPWM-DTC scheme for 3×5 DMC fed FPIM drive is validated through experiments. The necessary laboratory test setup is shown in Fig. 15. It comprises a 3×5 DMC connected to an FPIM, which further couples to a separately excited dc generator. Both the mechanical and electrical specifications of 3×5 DMC and FPIM are summarized in Table IV. For construction of 3×5 DMC, 15 bidirectional IGBT (SKM150GM12T4G) switches are utilized. Each IGBT is connected to SKYPER 32-PRO-R driver board without an interlocking option. A low-cost single-board computer with Zynq-7020 FPGA (FPGA-1) is used to generate IGBT switching pulses to operate 3×5 DMC. A dead band of 1.5 μs is given to each switching pulse to ensure the safe commutation of the bidirectional IGBT switches. Another dedicated Zynq-7020 based FPGA controller (FPGA-2) is used to implement the proposed controller. FPGA-1 and FPGA-2 are synchronized at 800 -MHz clock using IEEE-1588 v2 Protocol. However, the sampling time of both FPGA controllers set to 25 ns to achieve higher accuracy in dwell time calculations. Three grid-side voltage sensors (LEM LV25P), five FPIM-side current sensors (LEM LA-55P), and one speed encoder output are utilized as feedback signals for the inbuilt analog-to-digital converter of FPGA-1. The estimated torque and stator flux of FPIM can be measured through the digital-to-analog converter of FPGA-1. A protective system with a relay-operated contactor is used at the grid side of DMC just before the point-of-common coupling.

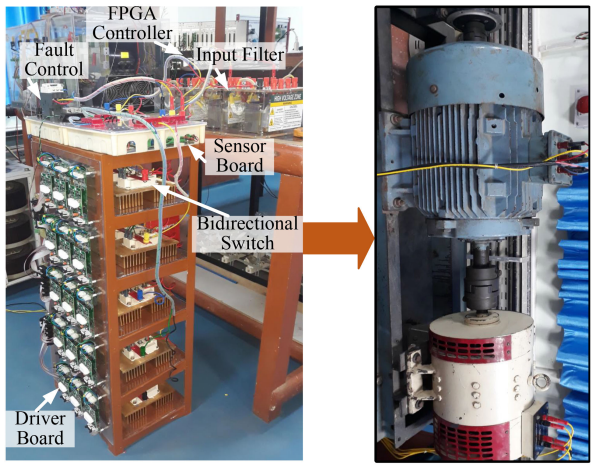

Fig. 15. Experimental setup of 3×5 DMC fed FPIM drive.

TABLE IV
Simulation and Experimental Parameters

FPIM Specifications
$5-\Phi$, $230\,V$, $3.8\,kW$, $1500\,rpm$, Nominal torque, $T_n = 22\,Nm$, Stator and rotor resistance, $R_s = 4.565\,\Omega$, $R_r = 9.989\,\Omega$, Leakage inductance in $\alpha\beta$ and xy plane, $L_{ls} = L_{lr} = 42.2\,mH$, $L_{ls3} = L_{lr3} = 5.7\,mH$, Mutual inductance in $\alpha\beta$ and xy plane, $L_m = 867.7\,mH$, $L_{m3} = 95.2\,mH$, Nominal flux: $\lambda_n = 0.867\,Wb$, Number of poles, $P = 4$, Moment of Inertia $J = 0.0772\,kgm^2$
Controller Specifications
Speed Controller: $k_p = 1.58$, $k_i = 3.75$, $T_{lim} = \pm T_n$; d-axis controller: $k_p = 5.1$, $k_i = 12.35$, $V_{lim}^d = \pm 1.5\,pu$; q-axis controller: $k_p = 100$, $k_i = 3000$, $V_{lim}^q = \pm 1.5\,pu$
3×5 DMC Parameters
$3-\Phi$ Input grid voltage, $V_g = 220\,V(rms)$, Line resistance, $R_l = 0.1\,\Omega$, Line inductance, $L_l = 0.15\,mH$, Smoothing resistance, $R_{sm} = 0.1\,\Omega$, Smoothing inductance, $L_{sm} = 0.15\,mH$, Filter resistance, $R_f = 0.1\,\Omega$, Filter inductance, $L_f = 8\,mH$

B. Experimental Results

The proposed SVPWM-DTC scheme was examined using three sets of test scenarios, and the corresponding results are shown in Figs. 16–23. During these experiments, the requirements for compensating the input power factor and maintaining a constant f_{sw} were investigated.

1) *Scenario-1:* FPIM speed variation of 0 to $80\%\,\omega_n$ at $25\%\,T_n$.

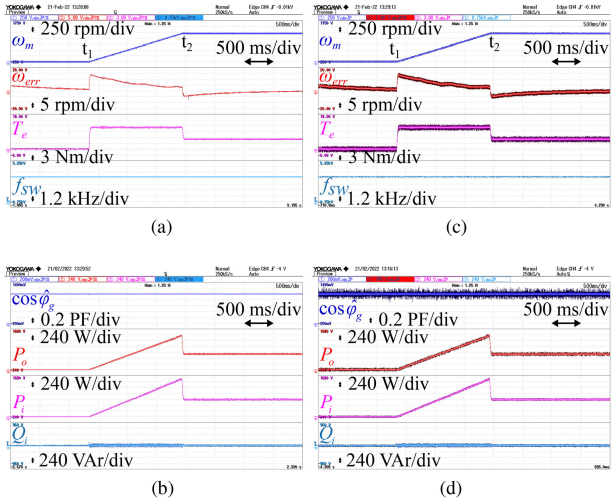

Fig. 16. Experimental results: FPIM drive performance at $T_L = 5$ Nm with step command of $\omega_m^* = 0$ to 1200 r/min (scenario-1) (a) Waveforms of ω_m, ω_{err}, T_e, f_{sw} with proposed controller. (b) Waveforms of $\cos\hat{\varphi}_g$, P_o, P_i, Q_i with proposed controller. (c) Waveforms of $\omega_m, \omega_{err}, T_e, f_{sw}$ for comparision study. (d) Waveforms of $\cos\hat{\varphi}_g$, P_o, P_i, Q_i for comparision study [21].

2) *Scenario-2:* Low speed and clockwise to anticlockwise (reversal) speed performance of FPIM drive during load torque variation from 5 to -5 Nm.
3) *Scenario-3:* $40\%\,T_n$ to $80\%\,T_n$ of load variation at $80\%\,\omega_n$ and vice versa.

The rotor speed (ω_m) of the motor, rotor speed error ($\omega_{\text{err}} = \omega_m^* - \omega_m$), electromagnetic torque (T_e), the stator currents $\left(i_o^{\alpha\beta}\right)$, and flux $\left(\hat{\psi}_s^{\alpha\beta}\right)$ trajectories in the $\alpha\beta$-frame are utilized to verify the controller effectiveness for FPIM drives. Additionally, the waveforms of the estimated input power factor $(\cos\hat{\varphi}_g)$, input active power (P_i), input reactive power (Q_i), output active power (P_o), and switching frequency f_{sw} specify the efficacy of the proposed SVPWM-DTC in regulating the input power quality of the 3×5 DMC.

1) Scenario-1: For this test scenario, FPIM drive is loaded to $25\%T_n$ (i.e., 5 Nm) at $t = t_1$ s. A step speed command of $\omega_m^* = 1200$ r/min is given to the controller at the same instant. From Fig. 16(a), it is observed that the desired speed of $\omega_m = 1200$ r/min is achievable by controller at $t = t_2$ s with a speed error of $\omega_{\text{err}} = \pm 15$ r/min. During the drive operation, the average switching frequency (f_{sw}) is maintained constant at 5 kHz. Fig. 16(b) provides the information on $\cos\hat{\varphi}_g$, P_o, P_i, and Q_i. $\hat{\varphi}_g$ is seen to be varied around $0°$, i.e., the proposed controller is able to achieve the unit input power factor operation. The input power P_i varies with the output power P_o requirement, considering an overall drive efficiency of 91.05%. The reactive power requirement from the grid is observed near to zero VAr that confirms nearly unit power factor operation of the DMC fed FPIM drive. The proposed control strategy is compared with FOC-[21], and corresponding results are shown in Fig. 16(c) and (d). With FOC-[21], the performance results have significantly higher tracking error and constitute higher ripple contents.

During this test scenario, the experimental results corresponding to $i_o^{\alpha\beta}$, i_o^{xy}, $\hat{\psi}_s^{\alpha\beta}$, and $\hat{\psi}_s^{xy}$ are provided in Fig. 17. The

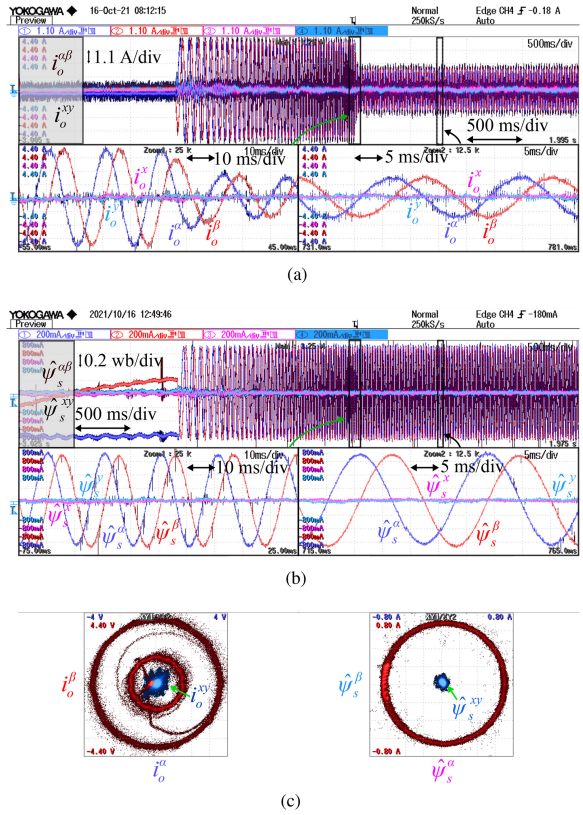

Fig. 17. Experimental results: FPIM stator current and flux performance during scenario-1. (a) Waveforms of $i_o^{\alpha\beta}$ and i_o^{xy}. (b) Waveforms of $\hat{\psi}_s^{\alpha\beta}$ and $\hat{\psi}_s^{xy}$. (c) Trajectories of Figs. 17(a) and 17(b).

zoomed portion of the results shown in Fig. 17(a) (bottom) and (b)(bottom) illustrate the transient and steady-state performance of the FPIM drive. The proposed VV-SVPWM confirms its superiority by nullifying the effect of the third harmonic components of the selected VVs on i_o^{xy}, and $\hat{\psi}_s^{xy}$. The trajectories in Fig. 17(c) further confirms the stable performance of the FPIM drive with the nullified effect of i_o^{xy} and $\hat{\psi}_s^{xy}$. Fig. 18(a) provides the instantaneous value of 3×5 DMC output line voltage (v_{AB}), output phase-A voltage (v_A), and output phase-A current (i_A). The instantaneous value of 3×5 DMC input phase-a current (i_{ia}), grid voltage (v_{ga}), and grid current (i_{ga}) are illustrated in Fig. 18(b). Zoomed portion of Fig. 18(a)(bottom) and (b)(bottom) show the transient and steady-state performance during scenario-I. The zoomed portion in Fig. 18(b)(bottom) indicates that v_{ga} and i_{ga} are in phase and denote a unit power factor operation of 3×5 DMC. As mentioned earlier, the proposed drive controller is also used to illustrate the reduced ripple in both output and input currents. Fig. 19(a)(top) shows the v_A and i_A of 3×5 DMC at $T_L = 5$ Nm and $\omega_m^* = 1200$ r/min. Corresponding fast Fourier transform (FFT) analysis is illustrated in Fig. 19(a)(bottom). Similarly, Fig. 19(b)(top) represents the waveform of i_{ia} and i_{ga} at $T_L = 5$ Nm and $\omega_m^* = 1200$ r/min. Also, related FFT analysis is depicted in 19(b)(bottom). A 12 and 6.5-kHz window are selected to evaluate the %THD performance for output and input current waveforms, respectively. Fig. 19(c)(top) indicates the common mode voltage and its effective magnitude during

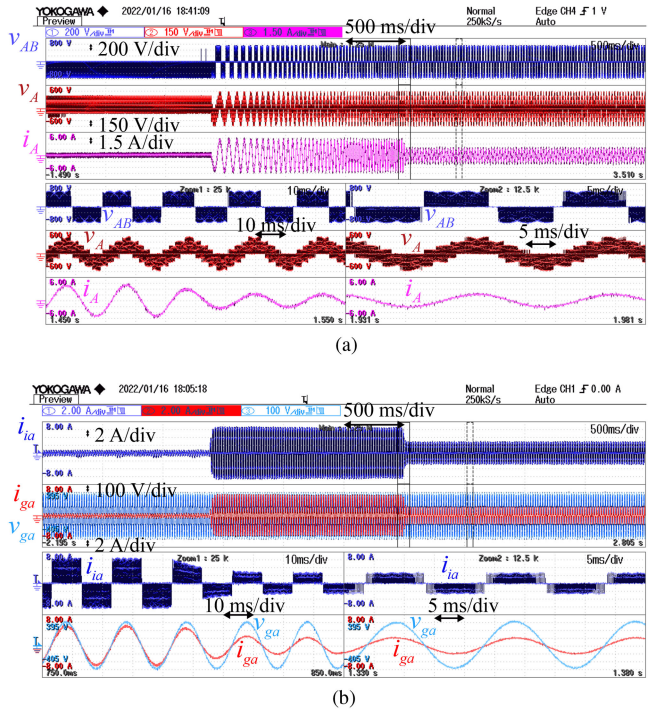

Fig. 18. Experimental results: FPIM stator current and flux performance during scenario-1. (a) Waveforms of v_{AB}, v_A, and i_A. (b) Waveforms of i_{ia}, i_{ga} and v_{ga}.

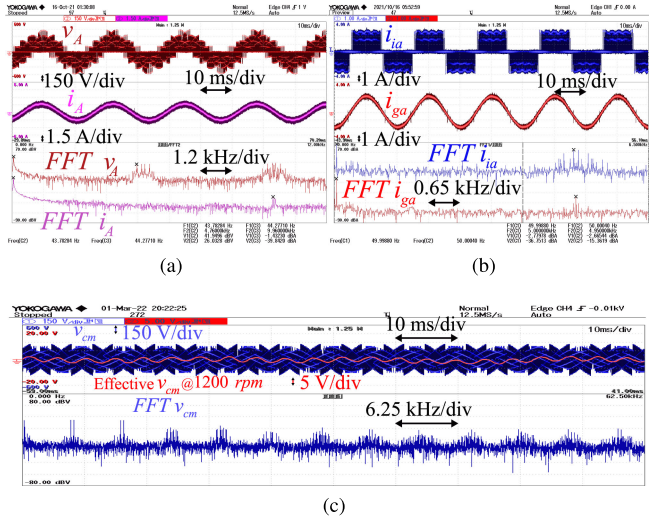

Fig. 19. FFT analysis of experimental waveforms at $T_L = 5$ Nm and $\omega_m^* = 1200$ r/min. (a) v_A and i_A with FFT analysis. (b) i_{ia} and i_{ga} with FFT analysis. (c) v_{cm} and effective v_{cm} with FFT analysis.

$\omega_m^* = 1200$ r/min. The effective magnitude of v_{cm} is quite low and varies in between ± 10 V. Fig. 19(c)(bottom) shows the FFT analysis of instantaneous values of v_{cm}. It can be seen from Fig. 19 that the FFT waveforms contain the harmonic side bands corresponding to the selected 5-kHz VV-SVPWM switching frequency.

2) Scenario-2: Fig. 20 illustrates the FPIM drive performance at various speeds with the suggested VV based SVPWM-DTC. FPIM is initially loaded to 5 Nm and a speed command

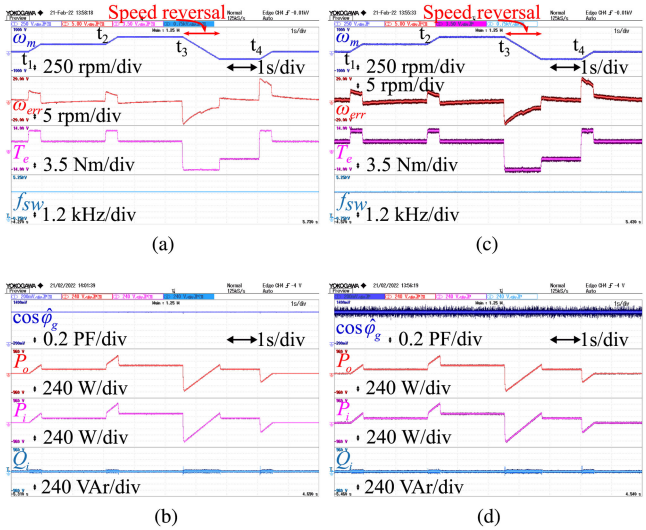

Fig. 20. Experimental results: FPIM drive performance at $T_L = 5$ Nm with low-speed and speed reversal operation (scenario-2). (a) With proposed controller. (b) With proposed controller. (c) Waveforms for comparision study. (d) Waveforms for comparision study.

of 300 r/min is given at $t = t_1$ s, as seen from Fig. 20(a). Then, the motor runs at 300 r/min until time $t = t_2$ s. The reference speed is set to 600 r/min at $t = t_2$ s and the speed is reversed at $t = t_3$ s considering a load torque of -5 Nm. Finally, the speed reference is set to 0 r/min at $t = t_4$ s. It is observed that ω_m tracks the reference speed with minimal ω_{err} and obtain the desired estimated torque, T_e. During such low speed and speed reversal operation, the drive switching frequency is maintained constant. As seen from Fig. 20(b), The input power factor angle is observed with less variation, i.e., $\pm 5^\circ$ during low speed operation and found around $\pm 1^\circ$ during higher speed of the FPIM drive. The performance of P_o, P_i and Q_i are observed in Fig. 20(b). It is observed that a bidirectional power flow is established during speed reversal (at $t_3 s$) and braking operation (at $t_4 s$). Scenario-2 is also tested for FOC-[21] and corresponding comparative results in Fig. 20(c)–(d) show the desired performance with high ripple content. The stator current $i_o^{\alpha\beta}$ and stator flux $\hat{\psi}_s^{\alpha\beta}$ waveforms in $\alpha\beta$-plane are presented in Fig. 21. The middle zoomed portion of Fig. 21 indicates the transient behavior during the low speed and speed reversal period. The stator flux trajectory in $\alpha\beta$-plane is observed as constant throughout the drive operation, as shown in Fig. 21(bottom). It is observed that the proposed SVPWM-DTC influences the overall performance of the drive in terms of reduced torque and current ripple.

3) Scenario-3: The dynamic performance of the FPIM drive through load change is observed in Fig. 22. Initially, the FPIM is loaded to 2.5 Nm and at $t < t_1$ s, a speed command of $\omega_m^* = 1200$ r/min is applied to the drive controller, as shown in Fig. 22(a). FPIM attains steady-state speed performance under loaded condition with the proposed SVPWM-DTC method. At $t = t_1$ s, a step change in load torque from $T_L = 2.5$ Nm to $T_L = 5$ Nm is applied, and then the FPIM is driven at a reduced load of $T_L = 2.5$ Nm at $t = t_2$ s. It is observed that

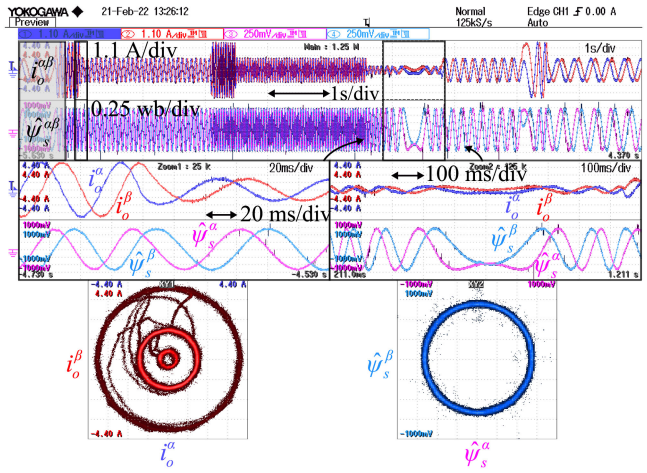

Fig. 21. Experimental results: FPIM drive stator current and flux performance during scenario-2.

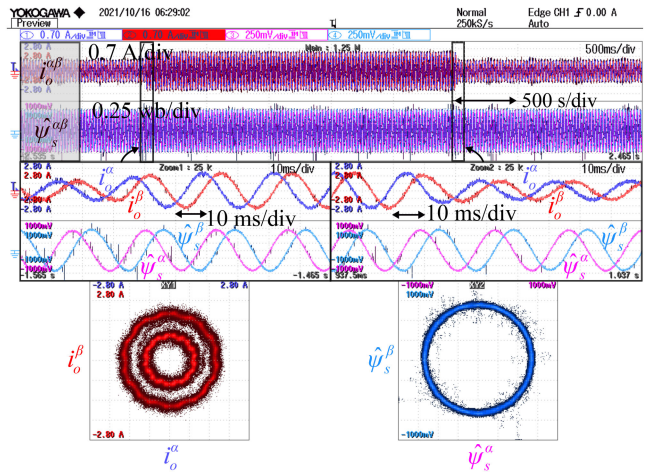

Fig. 23. Experimental results: FPIM drive stator current and flux performance during scenario-3.

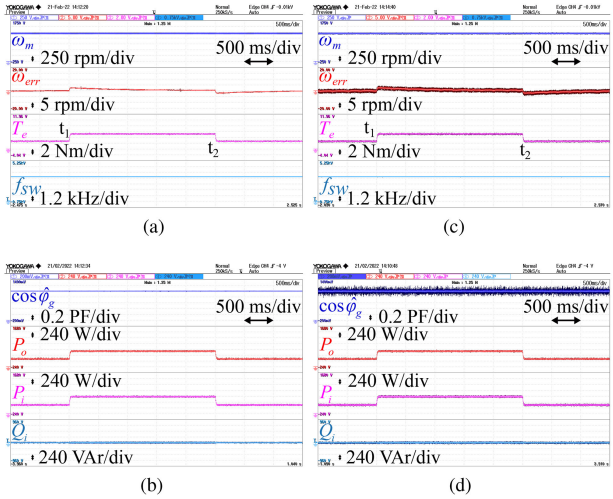

Fig. 22. Experimental results: FPIM drive performance during load torque variation at $\omega_m^* = 1200$ r/min (scenario-3). (a) With proposed controller. (b) With proposed controller. (c) Waveforms for comparision study. (d) Waveforms for comparision study.

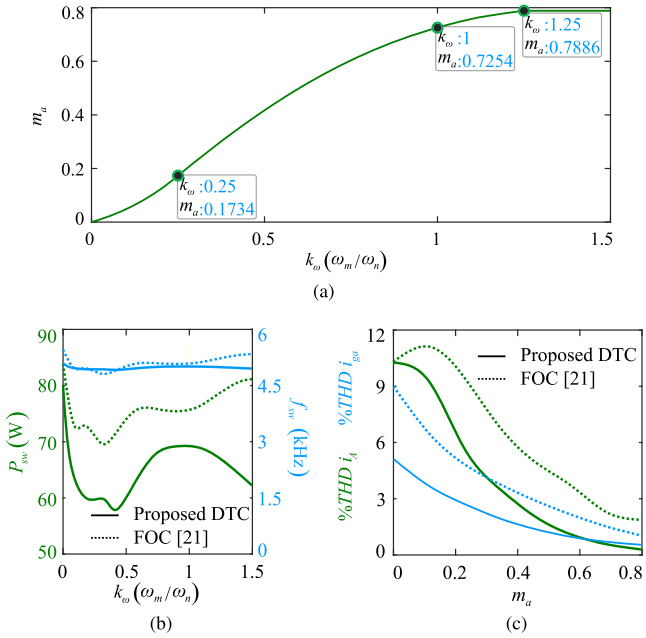

Fig. 24. Experimental results with comparative study at $T_L = 5$ Nm. (a) Voltage transfer ratio vs. k_ω. (b) f_{sw} and P_{sw} vs. k_ω. (c) %THD of i_A, and i_{ga} vs. m_a

the torque and speed of the FPIM drive track the reference values as expected with minimal error. The drive operation verifies that SVPWM-DTC maintains f_{sw} at 5 kHz. Fig. 22(a) illustrates the performance of the input power factor, input and output power flow of DMC. It can be seen that the input power factor of DMC is maintained near to unity. Scenario-3 is also tested for FOC-[21] and corresponding comparative results in Fig. 22(c)–(d) show the desired performance with high ripple content. The performance related to the stator currents and flux trajectories are similar to that of scenario-1, as shown in the bottom of Fig. 23. The proposed SVPWM-DTC has lower torque and current ripple due to the applied VV-SVPWM throughout the switching interval.

C. Comparative Study

This article compares the performance of the proposed SVPWM-DTC with FOC-[21]. The related speed and torque performances are presented in Figs. 16, 20, and 22 during all three scenarios. The corresponding descriptions are provided in Section IV-B. However, these discussions do not evaluate the switching loss and current THD performance during the change in FPIM speed or the voltage transfer ratio of the 3×5 DMC. Such illustrations are made in Fig. 24 and described here in this subsection.

1) Voltage Transfer Ratio Performance: Voltage transfer ratio (VTR) is considered as the modulation index (m_a) throughout this article. The impact of VTR m_a on % torque change and speed of the DMC fed FPIM drive is analyzed in Section III-B and illustrated graphically in Fig. 13. It is difficult to distinguish the direct relationship between m_a and the speed ratio k_ω (i.e., ω_m/ω_n) from this analysis. Hence, a direct relationship between

m_a and k_ω is demonstrated in Fig. 24(a). It can be seen that the VTR of the proposed SVPWM-DTC increases with the increase in rotor speed until attaining the maximum value of m_a, i.e., 0.7886.

2) DMC Switching Loss Performance: The 3×5 DMC has the bidirectional switches, which are controlled through SVPWM strategy with the hybrid commutation as in Section II. The development of the proposed SVPWM strategy assures minimal switching transition by maintaining the constant switching frequency (f_{sw}) of the overall drive. Fig. 24(b) denotes the f_{sw} and DMC switching loss (P_{sw}) activities with a wide range of FPIM speed variations. These performances are also compared with FOC-[21]. It can be observed that the f_{sw} is maintained constant for both methods due to the constant carrier frequency. However, the power loss P_{sw} in case of the proposed SVPWM-DTC is less in comparison to FOC-[21].

3) Current THD Performance: The proposed SVPWM-DTC and FOC-[21] are evaluated in terms of %THD of output phase-A current i_A and input phase-a grid current i_{ga}. It can be seen from Fig. 24(c) that the %THD performance of the proposed SVPWM-DTC is better than the FOC-[21] with increasing voltage transfer ratio m_a. As VTR is directly related to ω_m, it can also be concluded that the %THD performance of the proposed SVPWM-DTC is better than the FOC-[21] with increasing FPIM speed.

V. Conclusion

This article describes a VV-based SVPWM-DTC for a 3×5 DMC-fed FPIM drive. The third harmonic component in xy-plane is eliminated, while creating the SVPWM-VV sequence utilizing the volt-second balancing procedure. As the stator flux, torque, speed, and input power factor are all affected by SVPWM-VVs, a suitable analysis is done to design the look-up table to implement the proposed SVPWM-DTC scheme for the FPIM drive. Lower torque and stator current ripple are achieved with the proposed SVPWM-DTC method while retaining a constant average switching frequency. Additionally, the input power factor and grid current harmonic are both regulated by utilizing the same LUT. There are several test scenarios that are used to evaluate the effectiveness of the suggested scheme, including both steady-state and transient conditions. Based on the findings, it is concluded that the proposed SVPWM-DTC scheme achieved the desired objectives. The proposed drive control is merely useful for ship propulsion application in a ship microgrid. Additionally, this work can find its direct application in DMC fed high-power crane motor drives.

Acknowledgment

The authors would like to thank Dr. B. Chikondra for his cooperation in matrix converter prototype development and installation and S. Prakash, a Ph.D. scholar at IIT Patna, for his assistance during the collection of experimental data.

References

[1] E. Levi, R. Bojoi, F. Profumo, H. A. Toliyat, and S. Williamson, "Multiphase induction motor drives—A technology status review," *IET Electric Power Appl.*, vol. 1, no. 4, pp. 489–516, Jul. 2007.

[2] A. Tani, M. Mengoni, L. Zarri, G. Serra, and D. Casadei, "Control of multiphase induction motors with an odd number of phases under open-circuit phase faults," *IEEE Trans. Power Electron.*, vol. 27, no. 2, pp. 565–577, Feb. 2012.

[3] E. Levi, "Advances in converter control and innovative exploitation of additional degrees of freedom for multiphase machines," *IEEE Trans. Ind. Electron.*, vol. 63, no. 1, pp. 433–448, Jan. 2016.

[4] B. Chikondra, U. R. Muduli, and R. K. Behera, "An improved open-phase fault-tolerant DTC technique for five-phase induction motor drive based on virtual vectors assessment," *IEEE Trans. Ind. Electron.*, vol. 68, no. 6, pp. 4598–4609, Jun. 2021.

[5] A. Iqbal, S. M. Ahmed, and H. Abu-Rub, "Space vector PWM technique for a three-to-five-phase matrix converter," *IEEE Trans. Ind. Appl.*, vol. 48, no. 2, pp. 697–707, Mar./Apr. 2012.

[6] V. Naik N and S. P. Singh, "A novel interval type-2 fuzzy-based direct torque control of induction motor drive using five-level diode-clamped inverter," *IEEE Trans. Ind. Electron.*, vol. 68, no. 1, pp. 149–159, Jan. 2021.

[7] Q. Sun, J. Wu, and C. Gan, "Optimized direct instantaneous torque control for SRMS with efficiency improvement," *IEEE Trans. Ind. Electron.*, vol. 68, no. 3, pp. 2072–2082, Mar. 2021.

[8] M. Wang, D. Sun, W. Ke, and H. Nian, "A universal lookup table-based direct torque control for OW-PMSM drives," *IEEE Trans. Power Electron.*, vol. 36, no. 6, pp. 6188–6191, Jun. 2021.

[9] X. Wu, W. Huang, X. Lin, W. Jiang, Y. Zhao, and S. Zhu, "Direct torque control for induction motors based on minimum voltage vector error," *IEEE Trans. Ind. Electron.*, vol. 68, no. 5, pp. 3794–3804, May 2021.

[10] J. Xu, M. Odavic, Z.-Q. Zhu, Z.-Y. Wu, and N. Freire, "Switching-table-based direct torque control of dual three-phase PMSMs with closed-loop current harmonics compensation," *IEEE Trans. Power Electron.*, vol. 36, no. 9, pp. 10645–10659, Sep. 2021.

[11] D. Casadei, G. Serra, A. Tani, and L. Zarri, "Matrix converter modulation strategies: A new general approach based on space vector representation of the switch state," *IEEE Trans. Ind. Electron.*, vol. 49, no. 2, pp. 370–381, Apr. 2002.

[12] U. R. Muduli, B. Chikondra, and R. K. Behera, "Space vector PWM based DTC scheme with reduced common mode voltage for five-phase induction motor drive," *IEEE Trans. Power Electron.*, vol. 37, no. 1, pp. 114–124, Jan. 2022.

[13] M. Siami, D. A. Khaburi, M. Rivera, and J. Rodríguez, "A computationally efficient lookup table based FCS-MPC for PMSM drives fed by matrix converters," *IEEE Trans. Ind. Electron.*, vol. 64, no. 10, pp. 7645–7654, Oct. 2017.

[14] S. Mondal and D. Kastha, "Input reactive power controller with a novel active damping strategy for a matrix converter fed direct torque controlled DFIG for wind power generation," *IEEE Trans. Emerg. Sel. Top. Power Electron.*, vol. 8, no. 4, pp. 3700–3711, Dec. 2020.

[15] W. Deng, H. Li, and J. Rong, "A novel direct torque control of matrix converter-fed PMSM drives using dynamic sector boundary for common-mode voltage minimization," *IEEE Trans. Ind. Electron.*, vol. 68, no. 1, pp. 70–80, Jan. 2021.

[16] W. Deng and S. Li, "Direct torque control of matrix converter-fed PMSM drives using multidimensional switching table for common-mode voltage minimization," *IEEE Trans. Power Electron.*, vol. 36, no. 1, pp. 683–690, Jan. 2021.

[17] W. Deng, "Maximum voltage transfer ratio of matrix converter under DTC with rotating vectors," *IEEE Trans. Power Electron.*, vol. 36, no. 6, pp. 6137–6141, Jun. 2021.

[18] S. Payami and R. K. Behera, "An improved DTC technique for low-speed operation of a five-phase induction motor," *IEEE Trans. Ind. Electron.*, vol. 64, no. 5, pp. 3513–3523, May 2017.

[19] L. Zheng, J. E. Fletcher, B. W. Williams, and X. He, "A novel direct torque control scheme for a sensorless five-phase induction motor drive," *IEEE Trans. Ind. Electron.*, vol. 58, no. 2, pp. 503–513, Feb. 2011.

[20] U. R. Muduli, B. Chikondra, and R. K. Behera, "Direct torque control of 3x5 matrix converter fed five-phase IM drive using virtual vector concept," in *Proc. IEEE Appl. Power Electron. Conf. Expo.*, 2021, pp. 765–770.

[21] K. Rahman *et al.*, "Field-oriented control of five-phase induction motor fed from space vector modulated matrix converter," *IEEE Access*, vol. 10, pp. 17996–18007, 2022.
[22] U. R. Muduli and R. Kumar Behera, "High performance finite control set model predictive DTC for three-to-five phase direct matrix converter fed induction motor drive," in *Proc. 22nd IEEE Int. Conf. Ind. Technol.*, 2021, vol. 1, pp. 198–202.
[23] E. Levi, "Multiphase electric machines for variable-speed applications," *IEEE Trans. Ind. Electron.*, vol. 55, no. 5, pp. 1893–1909, May 2008.
[24] K. Kato and J.-I. Itoh, "Improvement of input current waveforms for a matrix converter using a novel hybrid commutation method," in *Proc. Power Convers. Conf. - Nagoya*, 2007, pp. 763–768.
[25] L. Wang *et al.*, "A finite control set model predictive control method for matrix converter with zero common-mode voltage," *IEEE Trans. Emerg. Sel. Topics Power Electron.*, vol. 6, no. 1, pp. 327–338, Mar. 2018.
[26] A. K. Sahoo, K. Basu, and N. Mohan, "Systematic input filter design of matrix converter by analytical estimation of RMS current ripple," *IEEE Trans. Ind. Electron.*, vol. 62, no. 1, pp. 132–143, Jan. 2015.
[27] H. M. Nguyen, H.-H. Lee, and T.-W. Chun, "Input power factor compensation algorithms using a new direct-SVM method for matrix converter," *IEEE Trans. Ind. Electron.*, vol. 58, no. 1, pp. 232–243, Jan. 2011.

Utkal Ranjan Muduli (Member, IEEE) received the B.Tech. in electrical and electronics engineering from Biju Patnaik University of Technology Odisha, Rourkela, Odisha, India, in 2011, the M.Tech. in electrical engineering from the Indian Institute of Technology Gandhinagar, Palaj, Gujarat, India, in 2014, and the Ph.D. in electrical engineering from the Indian Institute of Technology Patna, Bihta, Bihar, India, in 2022.

He was a Visiting Scholar and Research Associate, in 2019 and 2021, respectively, with the Department of Electrical Engineering and Computer Science, Khalifa University, Abu Dhabi, UAE, where he is currently working as Postdoctoral Research Fellow. His research interests include modulation strategies for multi-phase motor drives, matrix converters and its control, battery power management, and wireless power transfer.

Ranjan Kumar Behera (Senior Member, IEEE) received the B.Eng. degree in electrical engineering from the Regional Engineering College, Rourkela, Odisha, India, and the M. Tech. and Ph.D. degrees from the Indian Institute of Technology Kanpur, Kanpur, Uttar Pradesh, India, in 1998, 2003, and 2009, respectively.

He was a Visiting Scholar with the Energy Systems Research Center, Tennessee Technological University, Cookeville, TN, USA, in 2008. He has been a faculty member, since 2009, and is currently an Associate Professor with the Department of Electrical Engineering, Indian Institute of Technology Patna, Bihta, Bihar, India. During July 2016, he was a Visiting Research Collaborator with the Department of Electrical, Electronic and Computer Engineering, University of Pretoria, Pretoria, South Africa. His research interests include nonlinear control theory applications to power electronic converters, pulsewidth modulation techniques, and multiphase electric drive control.

Dr. Behera was the recipient of many national and international awards, such as Young scientists award in engineering sciences, DST, Government of India, 2001, Bhaskara Advanced Solar Energy Indo-U.S. Science and Technology Forum for Solar research in the USA, 2014, and was selected as the featured engineer of the globe 2015.

Khalifa Al Hosani (Senior Member, IEEE) received the B.Sc. and M.Sc. degrees in electrical engineering from the University of Notre Dame, Notre Dame, IN, USA, in 2005 and 2007, respectively, and the Ph.D. degree in electrical and computer engineering from Ohio State University, Columbus, OH, USA, in 2011.

He is currently an Associate Professor with the Department of Electrical and Computer Engineering, Khalifa University, Abu Dhabi, UAE. He is the Co-Founder of the Power Electronics and Advanced Sustainable Energy Center Laboratory, ADNOC Research and Innovation Center, Abu Dhabi, UAE. His research interests include a wide range of topics including nonlinear control, sliding mode control, control of power electronics, power systems stability and control, renewable energy systems modeling and control, smart grid, microgrid and distributed generation, and application of control theory to oil and gas applications.

Mohamed Shawky El Moursi (Senior Member, IEEE) received the B.Sc. and M.Sc. degrees from Mansoura University, Mansoura, Egypt, in 1997 and 2002, respectively, and the Ph.D. degree from the University of New Brunswick, Fredericton, NB, Canada, in 2005, all in electrical engineering.

He was a Research and Teaching Assistant with the Department of Electrical and Computer Engineering, UNB, from 2002 to 2005. He joined McGill University, Montreal, QC, Canada, as a Postdoctoral Fellow with the Power Electronics Group. He joined Vestas Wind Systems, Arhus, Denmark, with the Technology R&D, Wind Power Plant Group. He was with TRANSCO, Abu Dhabi, UAE, as a Senior Study and Planning Engineer. He is currently a Professor with the Electrical and Computer Engineering Department, Khalifa University of Science and Technology-SAN Campus, Abu Dhabi, UAE, and seconded to a Professor Position with the Faculty of Engineering, Mansoura University, Mansoura, Egypt, and is currently on leave. He was a Visiting Professor with the Massachusetts Institute of Technology, Cambridge, MA, USA. His research interests include power system, power electronics, FACTS technologies, VSC-HVdc systems, microgrid operation and control, renewable energy systems (wind and PV) integration, and interconnections.

Dr. El Moursi is currently an Editor for IEEE TRANSACTIONS ON POWER DELIVERY, IEEE TRANSACTIONS ON POWER SYSTEMS, Associate Editor for IEEE TRANSACTIONS ON POWER ELECTRONICS, Associate Editor for IEEE TRANSACTIONS ON SMART GRID, Guest Editor for IEEE TRANSACTIONS ON ENERGY CONVERSION, Guest Editor-in-Chief for the special section between IEEE TRANSACTIONS ON POWER DELIVERY and IEEE TRANSACTIONS ON POWER SYSTEMS, Editor for IEEE POWER ENGINEERING LETTERS, Regional Editor for *IET Renewable Power Generation*, and Associate Editor for *IET Power Electronics Journals*.